THE JOURNAL OF PHYSICAL CHEMISTRY C
A JOURNAL OF THE AMERICAN CHEMICAL SOCIETY

pubs.acs.org/JPCC Article

# Kinetic Relevance of Surface Reactions and Lattice Diffusion in the Dynamics of Ce–Zr Oxides Reduction–Oxidation Cycles

Andrew Hwang, Jason Wu, Andrew "Bean" Getsoian, and Enrique Iglesia*

Cite This: J. Phys. Chem. C 2023, 127, 2936–2952 Read Online



**ABSTRACT:** Reduction–oxidation cycles in oxides are ubiquitous in oxygen storage and transport, chemical looping processes, and fuel cells. O-atom addition and removal are mediated by coupling reactions of oxidants and reductants at surfaces with diffusion of O-atoms within oxide crystals, with either or both processes as limiting steps. $CeO_2$–$ZrO_2$ solid solutions (CZO) are ubiquitous in practice. They are used here to illustrate general experimental strategies and reaction–diffusion formalisms for nonideal systems that enable assessments of the kinetic relevance of the steps that mediate O-atom addition and removal in these materials; these experiments are described within the context of models that describe the driving forces for reaction and diffusion rigorously in terms of oxygen chemical potentials ($\mu_O$). These strategies assess the rate consequences of varying the fluid phase redox potential, through changes in the identity and pressures of the reactants and products used in redox cycles ($O_2$; $CO/CO_2$; $H_2/H_2O$; $N_2O/N_2$), of introducing dispersed metal nanoparticles that capture and react lattice O-atoms in CZO using CO or $H_2$, and of imposing intervening dwells without reaction within redox cycles. O-removal rates depend on reductant pressures, even when $CO/CO_2$ and $H_2/H_2O$ ratios are chosen to maintain the same surface $\mu_O$ if surface reactions were quasi-equilibrated. These data, taken together with significant rate enhancements in O-removal when Pt nanoparticles are present at CZO crystal surfaces and with similar rates before and after inert dwells, demonstrate that reduction rates by both CO and $H_2$ are limited by surface reactions without the presence of consequential spatial gradients in $\mu_O$ within CZO crystals. In contrast, O-addition rates to partially reduced CZO crystals are similar for $N_2O$ and $O_2$ reactants and are not affected by the presence of Pt nanoparticles; O-addition rates are significantly higher after intervening inert dwells during CZO oxidation, indicative of spatial gradients in $\mu_O$, which relax during nonreactive periods. These methods and models, illustrated here for CZO redox cycles at conditions relevant to oxygen storage practice, allow systematic assessments of the kinetic relevance of lattice diffusion and surface reactions for systems that use solids for the reversible storage and release of atoms, irrespective of the identity of the solids or the atoms (e.g., O, H, N, and S).

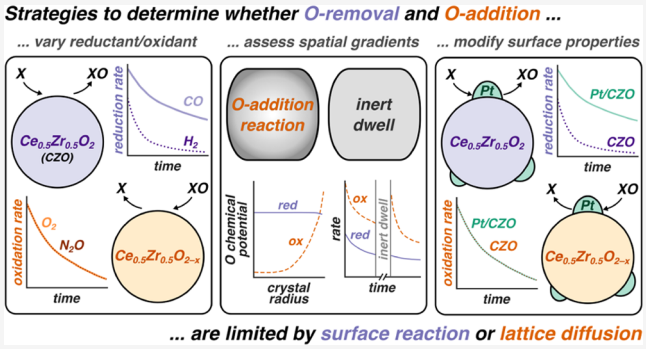




## 1. INTRODUCTION

Reducible oxides can exchange their O-atoms and electrons via chemical reactions with molecules present in a contacting fluid phase.[1−7] Reductants can react with an O-anion at oxide surfaces to form an anion vacancy that can be subsequently replenished via reactions with oxidants or through lattice diffusion of O-anions from within oxide crystals. The rates of O-removal and O-addition can be limited by either surface reaction rates, lattice diffusion rates, or both processes. The dynamics of these processes reflect the metal–oxygen bond strengths and redox potentials of the metal cations in a given oxide because reaction and transport events involve the formation and cleavage of M–O bonds and reduction–oxidation cycles of metal cations. The bond strengths and redox potentials depend on oxide composition and on its bulk structure and crystallite size, the number and type of defects, and the extent of reduction ($\xi_{red}$) from its stoichiometric form; the latter is most accurately reported as the fraction of the removable O-atoms that have been removed. For ceria-zirconia (CZO), one O-atom is removable for every four units of $Ce_{0.5}^{IV}Zr_{0.5}O_2$ such that a $\xi_{red}$ value of unity corresponds to full reduction to $Ce_{0.5}^{III}Zr_{0.5}O_{1.75}$.

Cerium oxides are reducible; they are useful in practice as electrolytes in solid oxide fuel cells[8−13] and as oxygen "buffers" that release and store oxygen during rich–lean cycles in automotive catalysis.[14−19] Three-way catalytic systems exploit the redox and transport properties of CZO solids to dampen fluctuations in the oxidation potential of effluent streams

Received: November 19, 2022
Revised: January 10, 2023
Published: February 1, 2023

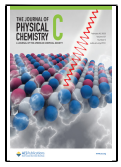




https://doi.org/10.1021/acs.jpcc.2c08117
J. Phys. Chem. C 2023, 127, 2936–2952

during cycling of fuel–air ratios; the Zr component in solid solutions provides structural integrity at extents of reduction that otherwise lead to phase transitions and large changes in solid density. In such processes, hydrocarbons and CO from fuel-rich ($O_2$-deficient) streams consume O-atoms in CZO and the vacancies formed react with $O_2$ during lean cycles. The Ce–O and Zr–O bond strengths and the redox properties of CZO solid solutions, and thus the rates at which they accept and release O-atoms, depend on the Ce/Zr ratio,[11,16,20−23] the crystal structure,[16,17,22] the local arrangement of Ce and Zr cations within the lattice,[16,17,24] the density of point defects,[25−27] and the extent of reduction during cycling.[11,20−23,28] The consequences of these CZO properties for O-atom diffusivity and reactivity must be interpreted based on kinetic and mechanistic models of surface reactions and lattice diffusion, details that are also essential to predict the dynamics of oxygen storage and release. Of specific relevance to the fidelity of such models is an assessment of the extent to which these rates reflect those of surface reactions or lattice transport.

This study examines such kinetic relevance of surface reactions and lattice diffusion using several types of experiments that are interpreted using reaction-transport formalisms (developed in Section 2.3); these treatments lead to rigorous descriptions of spatiotemporal profiles in O-content throughout CZO crystals and along packed beds and of the rates of addition and removal of O-atoms. One type of experiment (Section 3.1) probes to what extent O-atom removal/addition rates reflect only lattice diffusion rates; in such cases, experiments with reactant mixtures that would lead to the same surface O-atom chemical potentials (via equilibration at surfaces) would lead to similar rates of O-atom removal/addition, irrespective of the specific contacting pressures or the identity of the reductants and oxidants in such mixtures. Another type of experiment (Section 3.2) probes the consequences of inert "dwell" periods, during which lattice diffusion is able to equilibrate O-depleted (during reduction) or O-rich (during oxidation) in near-surface regions via O-atom diffusion from (or to) the bulk of CZO crystallites, on the O-atom removal (or addition) rates. A third type of experiment (Section 3.3) addresses how Pt nanoparticles at CZO surfaces affect O-atom removal and addition via processes that must recognize the kinetic relevance of surface reactions, given that such nanoparticles are exclusively present at CZO surfaces.

These experiments, taken together with the reaction-transport formalisms used to interpret them, demonstrate that O-removal by CO or $H_2$ is limited by surface reactions; these rates differ for $CO/CO_2$ and $H_2/H_2O$ mixtures that would lead to identical diffusional driving forces if surface reactions were equilibrated (i.e., if diffusional processes would solely limit rates). O-removal rates were unaffected by inert dwell periods, indicative of the absence of kinetically significant gradients in O-atom chemical potential throughout CZO crystals during contact with CO or $H_2$ reductants, which would have been unaffected, in fact, by the presence of Pt nanoparticles at CZO surfaces.

A similar experimental strategy shows that O-atom addition from $O_2$ and $N_2O$ to O-depleted CZO crystals is faster than O-depletion and becomes limited by diffusion as a result of very fast (and quasi-equilibrated) surface reactions (Section 3.4). O-addition rates from $O_2$ and $N_2O$ (expected to differ in surface reactivity) show similar temperature dependences. Dwell periods in an inert environment led to rates of O-atom addition by $N_2O$ that were initially higher after the dwell than before, as a result of intervening migration of O-atoms in the bulk, which dampens intracrystal gradients inherent in diffusion-limited systems. The presence of Pt nanoparticles at CZO surfaces did not influence O-addition rates by $N_2O$. In each case, these findings and trends contrast those observed during O-removal, a process that is limited by surface reactions of O-atoms with CO or $H_2$ instead of bulk lattice diffusion of O-atoms.

These strategies, illustrated here to determine the extent to which surface reactions or bulk diffusion limits CZO reduction–oxidation rates, are applicable in general to chemical looping,[6] thermochemical energy storage,[29,30] selective oxidations using lattice O-atoms (instead of $O_2$),[31] and reduction of molecules (e.g., $CO_2$ and $H_2O$) by donation of their O-atoms to vacancies in oxides,[32] for which such details are also essential for design and practice and for accurate descriptions of their function.

## 2. METHODS

**2.1. Characterization and Preparation of Ceria-Zirconia (CZO) Solid Solutions and CZO-Supported Pt (Pt/CZO).** A CZO sample was supplied by the Ford Motor Company before and after treatments intended to simulate extended use in the rich–lean cycles of automotive exhaust. It involved sequential treatments in reducing (1% $H_2$, 3% CO in $N_2$) and oxidizing (4% $O_2$, in $N_2$) environments at 1133 K (240 cycles in 16 h). X-ray fluorescence data (PANalytical Zetium XRF Spectrometer) gave a Ce/Zr ratio of 0.94 and trace Hf and Y concentrations (<1% at). X-ray diffractograms (Figure S1a; Supporting Information (SI); Rigaku Miniflex II diffractometer; Cu K$\alpha$; $\lambda$ = 1.5406 Å) gave the expected fluorite structure[33,34] and a cubic lattice constant (0.52909 nm) reported previously for $Ce_{0.5}Zr_{0.5}O_2$ (0.529,[20] 0.534,[23] 0.529,[33] and 0.533 nm[34]). Line breadth analysis using the Scherrer equation and the (220) line (at $2\theta = 49°$) gave mean crystallite diameters of 9.6 nm. The Raman spectrum (Figure S1b; SI; Renishaw InVia Raman spectrometer; Nd:$YVO_4$ 532 nm source; 10 mW power; spectral resolution of 4 $cm^{-1}$) showed one strong band at 480 $cm^{-1}$ with broad shoulders centered at 310 and 630 $cm^{-1}$. The 480 $cm^{-1}$ band corresponds to the single $F_{2g}$ Raman-active mode of cubic fluorite CZO structures and the 310 and 630 $cm^{-1}$ shoulders to vibrations of tetragonal Zr-rich CZO solutions.[34−37] $N_2$ adsorption–desorption isotherms (77 K; ASAP 2420 Micromeritics) gave a surface area of 40 $m^2$ $g^{-1}$ on samples evacuated (<0.013 Pa) at 673 K for 6 h before $N_2$ uptake measurements; this measured surface area is 2.4 times smaller than that estimated for a spherical CZO crystal with a diameter of 9.6 nm (from line breadth analysis of XRD pattern) and a bulk density of 6.61 g $cm^{-3}$.

Pt/CZO (1% wt) sample was prepared by incipient wetness impregnation. The CZO sample described above was treated in flowing dry air (2.5 $cm^3$ $s^{-1}$ $g^{-1}$; Linde, Ultra Zero) at 873 K (0.033 K $s^{-1}$; Applied Test Systems 3210) for 1 h before impregnation. An aqueous platinum(IV) nitrate solution (15% wt, Alfa-Aesar) was diluted with deionized water and added to the CZO sample in an amount equal to its pore volume, and the solids were treated in static dry air at ambient temperature for 16 h, at 383 K (Lindberg/Blue M) for 1 h, and then in flowing dry air (2.5 $cm^3$ $s^{-1}$ $g^{-1}$) at 873 K (0.033 K $s^{-1}$) for 1 h.


https://doi.org/10.1021/acs.jpcc.2c08117
J. Phys. Chem. C 2023, 127, 2936−2952

A CZO sample similar in composition and crystal structure to that above was prepared using sol−gel methods[38−40] to ensure that the conclusions for the CZO sample described above, but crystallized using undisclosed methods, were the same as for a sample of known provenance and prepared by well-described procedures. This procedure involved the dissolution of $Zr(OCH(CH_3)_2)_4$ (Sigma-Aldrich, ≥99.9%) in ethanol (Calbiochem, nondenatured, ≥99.5%) by magnetic stirring at 333 K for 2 h to give a 0.064 M solution of Zr. The same volume of a 0.064 M $(NH_4)_2Ce(NO_3)_6$ (Fluka, ACS Reagent) solution in deionized water (≥18.2 MΩ cm) was added to the $Zr(OCH(CH_3)_2)_4$ solution and stirred magnetically at 333 K for 2 h. Citric acid (Sigma-Aldrich, ACS Reagent) was then added to the solution (in a 2:1 citric acid/metal cation ratio) and stirred at 333 K for 2 h. Ethylene glycol (Fisher, Certified ACS) was then added (2:1 ethylene glycol/metal cation ratio) and stirred at 333 K for 2 h and then at 353 K for 24 h.

These procedures led to a cream-colored gel that converted to a brown-orange powder after treatment in static dry air at 433 K for 18 h. Pale yellow solids formed upon subsequent treatment in flowing dry air (0.56 $cm^3\ s^{-1}\ g^{-1}$) at 723 K (0.033 K $s^{-1}$) for 2 h and then at 1123 K (0.033 K $s^{-1}$) for 2 h. X-ray fluorescence spectra gave a Ce/Zr ratio of 1.0 with traces of Hf (<0.5% at); X-ray diffractograms (Figure S1a; SI) gave the expected fluorite structure and a mean crystal diameter of 12 nm (from line breadth analysis, as described above). The Raman spectrum (Figure S1b; SI) was similar to that of the CZO sample supplied by Ford, and $N_2$ uptakes at 77 K gave a surface area of 9.6 $m^2\ g^{-1}$, a value 7.9 times smaller than that estimated for 12 nm CZO spheres.

**2.2. O-Atom Removal and Addition Rates on CZO and Pt/CZO.** CZO and Pt/CZO powders were pressed, crushed, and sieved to retain 180−250 μm aggregates. They were mixed (0.01−0.1 g) with quartz granules (180−250 μm, 5−25 mass ratios of quartz to CZO or Pt/CZO) to avoid axial and radial temperature gradients and placed within a quartz "U"-tube cell (0.4 cm i.d.) with quartz wool at each end of the bed. These quartz granules (Sigma-Aldrich, ≥99.995%) were washed in 2 M $HNO_3$(aq) (10 mass ratio of solution to quartz), rinsed thrice with deionized water (200 mass ratio of water to quartz), treated in flowing dry air (0.67 $cm^3\ s^{-1}\ g^{-1}$) at 1123 K (0.042 K $s^{-1}$) for 12 h, and sieved to retain 180−250 μm granules. The cell was held within a resistively heated furnace (National Element FA120). Temperatures were maintained using an electronic controller (Watlow 96) and monitored using a K-type thermocouple (Omega) affixed to the outer surface of the cell at the axial midpoint of the sample bed.

Samples were treated in flowing 20 kPa $O_2$ (20% $O_2$/He; Linde, certified standard; 6.67−66.7 $cm^3\ s^{-1}\ (g\ CZO)^{-1}$) at 1000 K (0.05 K $s^{-1}$) for 1 h, then brought to the target temperature (340−798 K), and flushed with He (Linde, ≥99.999%) for longer than 1 h before exposure of stoichiometric CZO (or Pt/CZO) samples to the reactants (CO or $H_2$) used for O-removal. For O-addition experiments, samples were treated similarly (flowing 20 kPa $O_2$ at 1000 K for 1 h), but then exposed to flowing 5.0 kPa $H_2$ (mixture of He and 19.8% $H_2$/He; Praxair, certified standard; 6.67−66.7 $cm^3\ s^{-1}\ (g\ CZO)^{-1}$) at 1000 K for 2 h, and held in He flow (6.67−66.7 $cm^3\ s^{-1}\ (g\ CZO)^{-1}$) at 1000 K for 1 h, before bringing samples to either the target temperature (350 K) for isothermal experiments or the initial temperature (233 K) for temperature-ramping experiments and then exposing the reduced CZO (or Pt/CZO) to the oxidants ($O_2$ or $N_2O$) used in O-addition experiments. Subambient temperatures were achieved using the effluent from a liquid $N_2$ Dewar.

The inlet streams used in these experiments consisted of He, 5.06% Ar/He (Praxair, certified standard), 10.1% CO/He (Praxair, certified standard), 19.8% $H_2$/He, 5.0% $CO_2$/Ar (Praxair, certified standard), $H_2O$ (deionized, ≥18.2 MΩ cm), 3.0% $N_2O$/3.0% Ar/He (Praxair, certified standard), 2.0% $O_2$/He (Praxair, certified standard), and 20% $O_2$/He. Flow rates were metered using electronic mass flow controllers (Porter 201) for gases and a syringe pump (KD Scientific 200) for $H_2O$, which was vaporized at 373 K as it mixed with a flowing gas stream and transferred to the sample cell and the analytical systems through heated transfer lines (≥373 K). Inlet and outlet streams were speciated using an infrared analyzer (MKS Multi Gas Analyzer 2030) and a residual gas analyzer (Leybold Inficon Transpector 2.0). O-addition experiments with $N_2O$ were carried out by condensing unreacted $N_2O$ after the cell using a volume held at 77 K to allow $N_2$ products to be measured without significant contributions by $N_2O$ fragments in the residual gas analyzer; $N_2O$ concentrations were continuously measured using a split stream that bypassed the $N_2O$ condenser using the infrared analyzer.

**2.3. Reaction−Diffusion Formalisms for the Removal/Addition of O-Atoms from/to CZO.** O-atoms/O-vacancies are removed from CZO via reactions with reductants/oxidants at the crystal surface, which are then restored by O-diffusion from/into the lattice bulk. Either rate can limit CZO reduction/oxidation rates, but both rates would be simultaneously relevant only through fortuitous circumstances brought forth by a confluence of conditions, reductant/oxidant identity, and CZO surface-to-volume ratios. The relative kinetic relevance of these two processes depends not only on the identity and concentration of the reductant/oxidant and the CZO surface-to-volume ratio but also on the extent of reduction ($\xi_{red}$). CZO (and $CeO_2$) exhibit highly nonideal thermodynamics[10−12,20−23,28,41,42] with Gibbs free energies for O-removal that increase strongly as O-atoms are removed, and this nonideal behavior plausibly also affects the mobility and the reactivity of remaining O-atoms/O-vacancies such that they also depend strongly on $\xi_{red}$, as predicted by (linear) free energy relationships.[43] These effects become discernible and "separable" only by considering chemical and transport dynamics driven by gradients in chemical potential that are pertinent for thermodynamically nonideal systems, for which the mobility and reactivity of O-atoms depend sensitively on the extent of reduction.

The temporal (in time, $t$) and spatial (in general coordinates, $x$) evolution of O-atom concentration within a CZO crystal is given by

$$\frac{\partial C_O}{\partial t} = -\nabla \cdot J_O = \nabla \cdot (\sigma_O C_O \nabla \mu_O) \quad (1)$$

with $C_O$ and $J_O$ denoting the concentration and diffusion flux of O-atoms, respectively. The flux is proportional to the product of the chemical potential gradient of the diffusing species (O-atoms; $\nabla\mu_O$) and their concentration, with the proportionality constant defined as the O-atom mobility ($\sigma_O$).[44−47] The nonideal thermodynamics dictate that eq 1 be expressed in terms of $\mu_O$, the value of which is uniform


https://doi.org/10.1021/acs.jpcc.2c08117
J. Phys. Chem. C 2023, 127, 2936−2952

within CZO crystals at the initial time ($t = 0$) of the reduction and oxidation experiments and corresponds to that for stoichiometric CZO ($Ce_{0.5}Zr_{0.5}O_2$; $\mu_{O,0}$) and partially reduced, and subsequently annealed, CZO (e.g., $Ce_{0.5}Zr_{0.5}O_{1.83}$, see Section 3.4), respectively. The use of spherical coordinates creates a point of symmetry at the radial center of the CZO crystal ($r = 0$) where the net flux is zero ($(\nabla\mu_O)|_{r=0} = 0$). At CZO crystal surfaces ($r = R_p$), the diffusion flux equals the net (areal) rate of O-atom removal via surface reaction ($r_O^A$)

$$J_O\Big|_{r=R_p} = r_O^A\Big|_{r=R_p} \tag{2}$$

This boundary condition determines whether surface reactions are rate-limiting or in quasi-equilibrium such that diffusion is rate-limiting. Such assessments require specifying the functional forms for both terms in eq 2 and then scaling the system variables ($\mu_O$ and $r$). This nondimensionalization reveals the system parameters that affect the relative kinetic relevance of reaction and diffusion, and an asymptotic analysis of the resulting dimensionless form of eq 2 shows the limiting behavior for reaction- and diffusion-limited systems. The treatment that follows uses spherical CZO crystals, but other geometries can be derived from the results by simply defining a characteristic length scale given by the volume-to-surface ratio for each geometry.[48]

The flux at CZO crystal surfaces ($J_O$ in eq 2) is proportional to the O-atom mobility ($\sigma_O$), its concentration ($C_O$), and the gradient of chemical potential that provided the rigorous driving force for diffusion in thermodynamically nonideal systems ($-\nabla\mu_O$) at the surface ($r = R_p$)

$$J_O\Big|_{r=R_p} = -\left(\sigma_O C_O \frac{\partial\mu_O}{\partial r}\right)\Bigg|_{r=R_p} = -\left(\frac{\sigma_O RT}{R_p} C_O \frac{\partial\hat{\mu}_O}{\partial\hat{r}}\right)\Bigg|_{\hat{r}=1} \tag{3}$$

The value of $\sigma_O$ can depend on $C_O$ and therefore on $\xi_{red}$. The nondimensionalization in eq 3 scales distance by the crystal radius ($\hat{r} = r/R_p$) and uses the relation between $\mu_O$ and O-atom thermodynamic activity ($a_O$) to define a dimensionless chemical potential ($\hat{\mu}_O$)

$$\hat{\mu}_O = \frac{\mu_O - \mu_{O,0}}{RT} = \ln\left(\frac{a_O}{a_{O,0}}\right) = \ln\left(\frac{\gamma_O C_O}{C_{O,0}}\right) \tag{4}$$

where $R$ is the gas constant, $T$ is temperature, $\gamma_O$ is the activity coefficient for O-atoms, and $C_{O,0}$ and $a_{O,0}$ are the concentration and activity of O-atoms, respectively, for stoichiometric $Ce_{0.5}Zr_{0.5}O_2$ (corresponding to $\mu_{O,0}$), which here is taken to have an activity coefficient of unity ($\gamma_{O,0} = 1$). The functional form for diffusion flux (eq 3) remains the same between mathematical descriptions for O-atom removal and that for O-atom addition (CZO reduction and oxidation, respectively); the flux of O-atoms at the crystal surface is positive for CZO reduction and negative for oxidation.

The net areal rate of O-atom removal at CZO crystal surfaces ($r_O^A$ in eq 2) is related to the net volumetric rate ($r_O^V$) via the volume-to-surface ratio ($V/A$), which is one-third of the crystal radius

$$r_O^A = \left(\frac{V}{A}\right) r_O^V = \left(\frac{1}{3}R_p\right) r_O^V \tag{5}$$

This net rate is equal to the forward rate for O-atom removal (CZO reduction, $r_{red}^V$) less the reverse rate (CZO oxidation, $r_{ox}^V$)

$$r_O^V = (r_{red}^V - r_{ox}^V) = r_{red}^V(1 - \eta_{red}) \tag{6}$$

which can be equivalently expressed in terms of $r_{red}^V$ and the approach-to-equilibrium for reduction ($\eta_{red} = r_{ox}^V/r_{red}^V$). The forward rate equation for O-atom removal ($r_{red}^V$) can be expressed as the product of a pseudo-first-order rate parameter ($k_{red}$), O-atom activity ($a_O = \gamma_O C_O$), and a generic function ($f_{red}$) which can depend on reductant and/or oxidant concentrations (e.g., CO and $CO_2$ pressures) and can be parameterized by rate and equilibrium parameters which, in turn, depend on $\xi_{red}$

$$r_O^A = \left(\frac{1}{3}R_p\right)(k_{red}\,\gamma_O\,C_O f_{red})(1 - \eta_{red}) \tag{7}$$

As for $\sigma_O$ in the flux (eq 3), the values of $k_{red}$ and $\gamma_O$ can depend on O-atom concentration and thus on $\xi_{red}$. The functional form for the net areal rate of O-atom removal (eq 7), like that for diffusion flux (eq 3), is unchanged whether the description is for CZO reduction or oxidation; the net rate of O-atom removal is positive for CZO reduction and negative for CZO oxidation.

Substituting eqs 3 and 7 into eq 2 gives the surface boundary condition in dimensionless form

$$-\left(\frac{\partial\hat{\mu}_O}{\partial\hat{r}}\right)\Bigg|_{\hat{r}=1} = \phi^2(1 - \eta_{red})|_{\hat{r}=1} \tag{8}$$

The parameter $\phi^2$ is defined as

$$\phi^2 = \frac{1}{3}\left(\frac{k_{red}\,\gamma_O f_{red}}{\sigma_O RT/{R_p}^2}\right)\Bigg|_{\hat{r}=1} \tag{9}$$

It represents the ratio of a volumetric rate for the surface reaction at conditions far away from equilibrium ($k_{red}\,a_O\,f_{red}$) to a maximum lattice diffusion rate per volume ($\sigma_O\,RT\,C_O/{R_p}^2$) at the crystal surface. It is analogous to the Thiele modulus used to describe diffusion-limited reactions in porous solids but, in this case, for diffusion (without reaction) within a solid crystal and reaction of the diffusing species (only) at outer crystal surfaces. This parameter $\phi^2$ determines the extent to which intracrystal gradients in oxygen chemical potentials ($\phi^2 \gg 1$) or surface reactions ($\phi^2 \ll 1$) limit O-removal/addition. The value of $\phi^2$ depends on the identity and concentration of the reductant (or oxidant) in the contacting fluid (through $f_{red}$), the diffusion distances (crystal size and shape, through $R_p$ (or volume to surface area, $V/A$); see eq 5), and temperature and extent of reduction (through their respective consequences for $k_{red}$, $\gamma_O$, $f_{red}$, and $\sigma_O$).

For $\phi^2$ values much smaller than unity, the term on the right-hand side of eq 8 also becomes much smaller than unity such that

$$-\left(\frac{\partial\hat{\mu}_O}{\partial\hat{r}}\right)\Bigg|_{\hat{r}=1} \to 0, \text{ for } \phi^2 \ll 1 \tag{10}$$


https://doi.org/10.1021/acs.jpcc.2c08117
J. Phys. Chem. C 2023, 127, 2936−2952

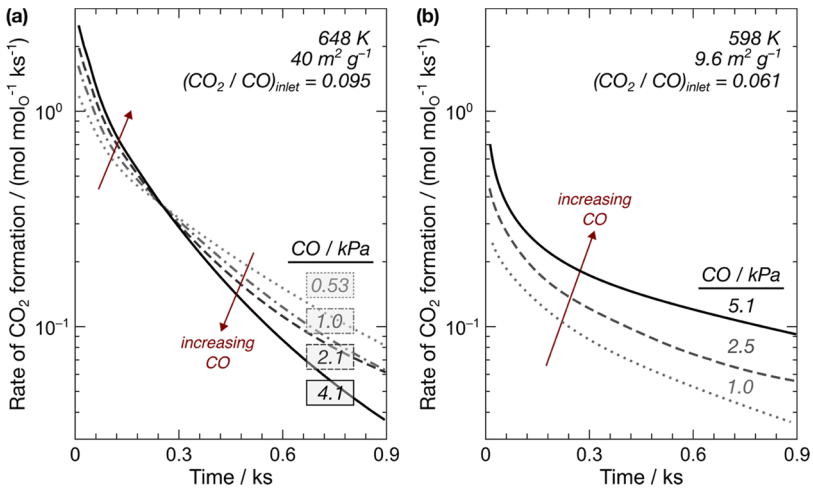


**Figure 1.** Rates of $CO_2$ formation per total removable oxygen (one O-atom per four units of $Ce_{0.5}{}^{IV}Zr_{0.5}O_2$) as a function of time for CO reactions with (a) $Ce_{0.5}Zr_{0.5}O_2$ (40 $m^2$ $g^{-1}$) at 648 K and different CO and $CO_2$ inlet pressures: (0.53 kPa CO, 0.045 kPa $CO_2$; dotted), (1.0, 0.099; dash-dotted), (2.1, 0.20; dashed), and (4.1, 0.41; solid) and (b) $Ce_{0.5}Zr_{0.5}O_2$ (9.6 $m^2$ $g^{-1}$) at 598 K and different CO and $CO_2$ inlet pressures: (1.0 kPa CO, 0.063 kPa $CO_2$; dotted), (2.5, 0.15; dashed), and (5.1, 0.31; solid).

The intracrystal chemical potential of O-atoms becomes spatially uniform as lattice diffusion becomes much faster than surface reaction ($\phi^2 \ll 1$). Thus, the absence of intracrystal spatial gradients in $\mu_O$ reflects a reaction-limited system.

For $\phi^2$ values much larger than unity, the product of the reciprocal of $\phi^2$ (i.e., $1/\phi^2$) and the term on the left-hand side of eq 8 becomes much smaller than unity such that

$$\eta_{red}|_{\hat{r}=1} \rightarrow 1, \text{ for } \phi^2 \gg 1 \tag{11}$$

The surface reaction reaches equilibrium when the forward and reverse rates become much larger than the rate of lattice diffusion ($\phi^2 \gg 1$). Such equilibration reflects a diffusion-limited system.

This mathematical description of the reaction−diffusion system can accommodate both O-removal and O-addition. An analogous formulation using the chemical potential of anion vacancies ($\mu_v$) instead of $\mu_O$ as the dependent variable can be more convenient, however, when describing experiments for O-atom addition. The resulting dimensionless form of the surface boundary condition, analogous to eq 8, is

$$-\left(\frac{\partial \hat{\mu}_v}{\partial \hat{r}}\right)\bigg|_{\hat{r}=1} = \psi^2(1 - \eta_{ox})|_{\hat{r}=1} \tag{12}$$

with the parameter $\psi^2$ defined analogously to $\phi^2$ (eq 9)

$$\psi^2 = \frac{1}{3}\left(\frac{k_{ox}\,\gamma_v f_{ox}}{\sigma_v RT/R_p{}^2}\right)\bigg|_{\hat{r}=1} \tag{13}$$

where $\sigma_v$ and $\gamma_v$ are the anion vacancy mobility and activity coefficient, respectively, and $k_{ox}$ and $f_{ox}$ are analogous to $k_{red}$ and $f_{red}$ but for O-atom addition (CZO oxidation). The same system variables that affect $\phi^2$ (reductant and oxidant concentrations, $R_p$, $T$, and $\xi_{red}$) also affect $\psi^2$, and an asymptotic analysis of eq 12 results in identical implications of the magnitude of $\psi^2$ on the relative kinetic relevance of reaction and diffusion, with $\psi^2 \ll 1$ and $\psi^2 \gg 1$ corresponding to, respectively, a reaction-limited system with negligible intracrystal spatial gradients in $\mu_v$ and a diffusion-limited system with (quasi)equilibrated surface reactions.

## 3. RESULTS AND DISCUSSION

**3.1. Surface Oxygen Chemical Potential as the Relevant Driving Force for Surface Reaction and Lattice Diffusion.** This section describes experiments for CZO reduction that probe the extent to which O-atom (O) removal by CO

$$CO + O \rightleftharpoons CO_2 \tag{14}$$

is limited by lattice diffusion of O-atoms. In such instances ($\phi^2 \gg 1$), surface reactions would be in quasi-equilibrium (eq 11), and the criterion for chemical reaction equilibrium requires that

$$\mu_O(t, r = R_p) = \mu_{CO_2} - \mu_{CO} = \mu^\circ_{CO_2} - \mu^\circ_{CO} + RT \ln\left(\frac{P_{CO_2}}{P_{CO}}\right) \tag{15}$$

where $\mu_i$, $\mu_i^\circ$, and $P_i$ (i = CO or $CO_2$) are the chemical potential, standard state chemical potential, and pressures of species i, respectively; pressures are used instead of fugacities because of the ideal nature of the contacting fluid phase. This equation gives surface O-atom chemical potentials as the difference in chemical potentials of $CO_2$ and CO at any given ratio of their pressures. For such diffusion-limited systems, O-removal rates at any time during transient reduction processes would depend only on the ($P_{CO_2}/P_{CO}$) ratio, but not on the magnitude of the pressures chosen to attain any given ratio, since only ratios appear in eq 15. The composition of the fluid phase appears only in the surface boundary condition (eq 15); neither the O-atom balance (eq 1), the initial condition ($\mu_O$ ($t$ = 0, $r$) = $\mu_{O,0}$), nor the boundary condition at the particle center ($(\nabla\mu_O)|_{r=0} = 0$) involve any knowledge about the reductant or oxidant concentrations.

Figure 1a shows $CO_2$ formation rates (normalized by removable O-atoms, those removed in $Ce_{0.5}{}^{IV}Zr_{0.5}O_2$ reduction to $Ce_{0.5}{}^{III}Zr_{0.5}O_{1.75}$; one O-atom per four $Ce_{0.5}{}^{IV}Zr_{0.5}O_2$) as a function of time at 648 K for experiments at the same inlet


https://doi.org/10.1021/acs.jpcc.2c08117
J. Phys. Chem. C 2023, 127, 2936−2952

$CO_2$/CO ratio (0.095) but different CO (0.53, 1.0, 2.1, 4.1 kPa) and $CO_2$ (0.045, 0.099, 0.20, 0.41 kPa) pressures on CZO (40 $m^2$ $g^{-1}$). These experiments would set the same oxygen chemical potential at surfaces if surface reactions were quasi-equilibrated and lattice diffusion was the sole rate-limiting process. This expectation is clearly contradicted by the data in Figure 1a, which show that the four sets of data are not coincident. The O-atom removal rates decrease with increasing time as O-atoms are consumed; at early times (and at equivalent values of $\xi_{red}$), rates increase sublinearly with increasing CO pressure as $CO_2$ pressure concomitantly increases. These trends reflect a surface reaction rate equation that is positive-order in CO and negative-order in $CO_2$. Surface reaction processes control, at least in part, O-removal rates at these conditions for this CZO sample.

This conclusion is contingent, however, on the significant depletion of O-atoms beyond the surface layer because, in such instances, rates would reflect (by definition) only the removal of surface O-atoms without any requirement for (or kinetic consequences of) lattice diffusion. On this CZO sample, surface O-atom depletion would correspond to an extent of reduction of 0.081 (assuming (111) CZO planes; 40 $m^2$ $g^{-1}$, 0.52909 nm lattice constant). The extents of reduction at 0.9 ks are all larger than 0.27, corresponding to more than 3.3 O-monolayers for these experiments. Consequently, the observed effects of $CO_2$/CO ratios reflect the kinetic relevance of surface reactions, unaffected by the preferential removal of only O-atoms at the surface layer of CZO crystals.

These observations parallel those for reactions on the other CZO sample (9.6 $m^2$ $g^{-1}$; sol−gel synthesis, Section 2.1; Figure 1b) at 598 K and the same inlet $CO_2$/CO ratio (0.061). The extents of reduction for all three of these reactions exceed that corresponding to 3.0 O-monolayers; thus, bulk O-atoms are necessarily removed in these reactions. The rate versus time curves for this CZO sample (Figure 1b; 9.6 $m^2$ $g^{-1}$), like those for the other CZO sample (Figure 1a; 40 $m^2$ $g^{-1}$), do not coincide, demonstrating once again that lattice diffusion is not the sole kinetically relevant step, even for CZO crystals with 4-fold lower surface areas.

The kinetic relevance of surface reaction steps is also consistent with the different O-removal rates with CO and $H_2$ as reductants when inlet $CO_2$/CO and $H_2O/H_2$ ratios are chosen to give the same O-atom chemical potential if their respective surface reactions were quasi-equilibrated (Figure 2). Gibbs free energies at 798 K[49] for these molecules in their gaseous form show that the chemical potential of O-atoms (in gaseous form and thus on surfaces in equilibrium with these mixtures) is the same when $P_{CO_2}/P_{CO}$ ratios are 4.2 times larger than $P_{H_2O}/P_{H_2}$ ratios. Figure 2 shows $CO_2$ (solid curve) and $H_2O$ (dashed curve) formation rates for CZO (40 $m^2$ $g^{-1}$) reduction with a 0.50 $CO_2$/CO ratio (0.26 kPa $CO_2$; 0.52 kPa CO) and a 0.12 $H_2O/H_2$ ratio (0.42 kPa $H_2O$; 3.6 kPa $H_2$), corresponding to equal chemical potentials of O-atoms if such mixtures were equilibrated at surfaces (−304 kJ $mol^{-1}$), as required if lattice diffusion was the sole kinetically relevant step. Yet, O-removal rates are smaller with $H_2O-H_2$ than $CO_2$−CO mixtures, in spite of reductant pressures that are higher with $H_2$ than with CO (3.6 vs 0.52 kPa). The identity and the concentration of the reductant matters, even when using reactant mixtures that would lead to the same O-chemical potentials if surface reactions were in quasi-equilibrium.

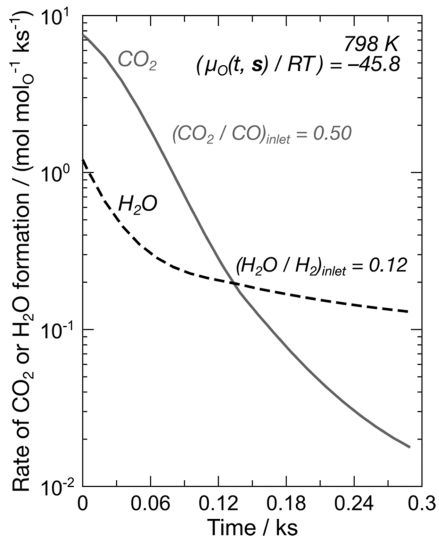


**Figure 2.** Rates (per removable O-atom) of $CO_2$ (solid curve) and $H_2O$ (dashed curve) formation as a function of time for reactions of (0.52 kPa CO, 0.26 kPa $CO_2$) and (3.6 kPa $H_2$, 0.42 kPa $H_2O$), respectively, with $Ce_{0.5}Zr_{0.5}O_2$ (40 $m^2$ $g^{-1}$) at 798 K. These $CO_2$/CO and $H_2O/H_2$ ratios give a surface oxygen chemical potential (eq 15) of −304 kJ $mol^{-1}$ (= −45.8($RT$)).

These results (Figures 1 and 2) demonstrate that O-atom removal cannot be solely limited by lattice diffusion, but they do not demonstrate the exclusive kinetic relevance of reactions of O-atoms with CO or $H_2$ at CZO surfaces. Next (Section 3.2), an experiment that exploits the formalism developed in Section 2.3 is used to show that O-atom chemical potentials within CZO crystals are essentially uniform and that surface reactions of CO and $H_2$ with O-atoms at surfaces represent the only limiting process during O-removal from CZO at temperatures relevant to automotive exhaust catalysis, solid oxide fuel cells, and chemical looping ($T \geq 500$ K).

**3.2. Consequences of Inert Dwell Periods for O-Removal Rates and Kinetic Relevance of Lattice Diffusion during O-Atom Removal by CO and $H_2$.** O-removal processes limited, at least in part, by lattice diffusion exhibit surface and bulk regions of CZO crystals that are not at thermodynamic equilibrium. A "dwell time" in an inert environment allows diffusion to bring surface and bulk regions closer to equilibrium, without concurrent removal of O-atoms from CZO crystals during the dwell. As a result, near-surface regions are brought to higher $\mu_O$ values than before the inert dwell. Restoring the reductant would then lead to higher O-removal rates than before the dwell in cases where lattice diffusion limits, even in part, such rates. When no such gradients exist and O-removal rates are solely limited by surface reactions, inert dwells would have no detectable effects on O-removal rates upon subsequent contact with reductants because surface and bulk regions would remain at equilibrium during O-removal.

These consequences are evident from the reaction−diffusion model described in Section 2.3 using a $\phi^2$ (eq 9) value of 10, which leads to significant spatial gradients within CZO crystals. Such an illustration of the consequences of a dwell period without O-removal also assumes that the CZO reduction reaction is far from equilibrium ($\eta_{red} \ll 1$) and that surface reaction rates ($r_{red}^V$, eq 7) are proportional to the thermodynamic activity of O-atoms ($a_O$); the latter is assumed, without


https://doi.org/10.1021/acs.jpcc.2c08117
J. Phys. Chem. C 2023, 127, 2936−2952

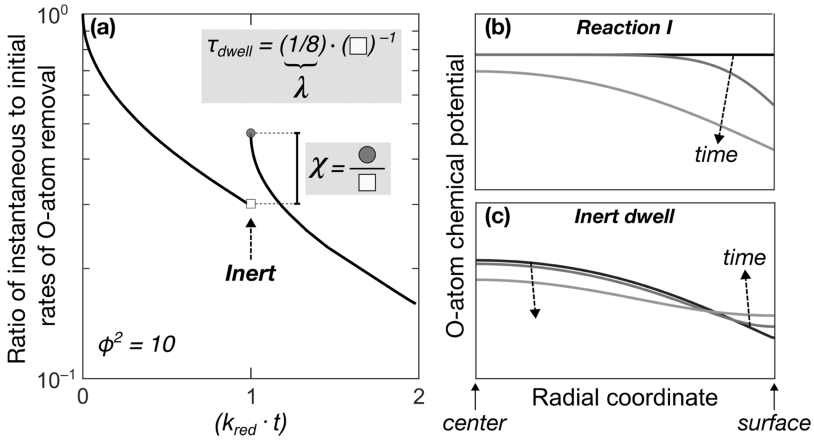


**Figure 3.** Results of an illustrative example (eqs 1, 8, and 16) that depicts the consequences of an intervening inert dwell period on O-atom removal rates for a diffusion-limited system ($\phi^2 = 10$). (a) Rates of O-atom removal, scaled by the rate at zero time, versus time, scaled by the inverse of $k_{red}$ (= 1 $ks^{-1}$). The ratio of the rate after (●) to that before (□) the inert dwell period is defined as $\chi$, and the duration of the inert dwell ($\tau_{dwell}$) is a fraction, defined as $\lambda$, of the inverse of the rate before the dwell period ($\square^{-1}$). (b, c) Chemical potential of O-atoms versus radial coordinate during the first O-atom removal reaction (Reaction I; b) and during the inert dwell period (inert dwell; c). The abscissa for the radial coordinate (b, c) spans from, left to right, the center to the surface of the CZO crystal.

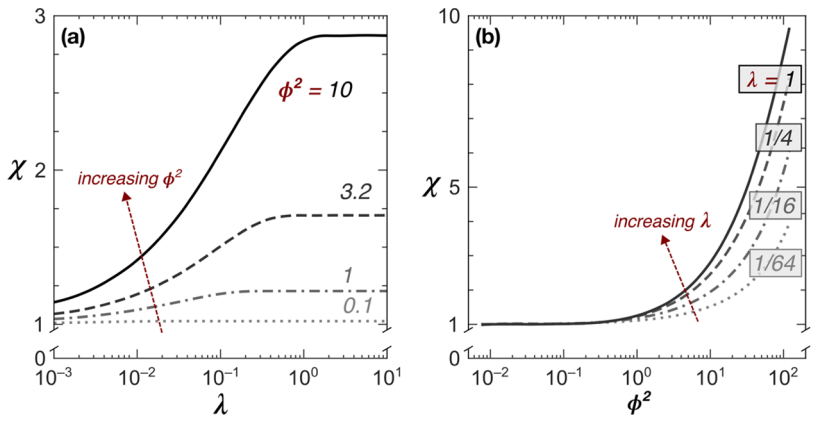


**Figure 4.** (a) Ratio of the O-atom removal rate after to that before an intervening inert dwell period ($\chi$, Figure 3) versus the dimensionless duration of the inert dwell period ($\lambda$, Figure 3); the solid, dashed, dash-dotted, and dotted curves correspond to $\phi^2$ (eq 16) values of 10, 3.2, 1, and 0.1, respectively. (b) Values of $\chi$ versus $\phi^2$ at $\lambda$ values of 1 (solid), 0.25 (dashed), 0.0625 (dash-dotted), and 0.015625 (dotted).

loss of generality and for illustrative purposes, to be proportional to the concentration of O-atoms ($C_O$) at any time and radial position. The $\phi^2$ value is then given by

$$\phi^2 = \frac{1}{3}\left(\frac{k_{red}}{\sigma_O RT/R_p^{\,2}}\right)\Bigg|_{\hat{r}=1} \tag{16}$$

For this example, the reaction duration, the length of time that CZO remained in contact with reductant before the inert dwell period, is set to the inverse of the first-order rate constant ($k_{red}$), and the dwell duration ($\tau_{dwell}$) is varied to examine how it affects the rate instantaneously upon reintroducing the reductant.

These simulations (for $\phi^2 = 10$) give O-atom removal rates that decrease with time in contact with reductants, as their concentration and chemical potential decrease (Figure 3a; Reaction I; ($k_{red}\ t$) = 0−1); here, rates are scaled by the initial rate (at $t = 0$) and time is scaled by the inverse of $k_{red}$ (= 1 $ks^{-1}$). The $\mu_O$ values at each crystal position are shown in Figure 3b at different times during contact with reductants; from the initially uniform $\mu_O$ profile, gradients emerge near the surface and extend into CZO crystals with increasing reaction time. At a $k_{red}\ t$ value of 1, the surface reaction rate is set to zero for a period of time ($\tau_{dwell}$) that is equal to a fraction (0.125) of the inverse of the O-atom removal rate instantaneously before the inert dwell period, a rate value indicated in Figure 3a by the open square (□). The ratio between the dwell duration ($\tau_{dwell}$) and the instantaneous characteristic timescale for O-atom removal (i.e., the inverse of the rate specified by the open square (□) in Figure 3a) is defined here as $\lambda$, which is set to 0.125 for the example in Figure 3. Figure 3c shows that spatial profiles of $\mu_O$ become gradually flatter during the inert dwell period and that values of $\mu_O$ increase with time at near-surface regions. Consequently, O-removal rates are higher when the reductant is again introduced (and surface reactions are allowed to occur) than before the dwell period (Figure 3a). The rate enhancement, defined as the ratio of rates after and before the inert dwell period, is defined as $\chi$; these two rates are depicted in Figure 3a by, respectively, the filled circle (●) and the open square (□).

The $\chi$ values depend on the severity of the spatial gradients ($\phi^2$) and the time allowed for such gradients to relax ($\lambda$; relative to the timescale for O-removal). Figure 4a shows that $\chi$


https://doi.org/10.1021/acs.jpcc.2c08117
J. Phys. Chem. C 2023, 127, 2936−2952

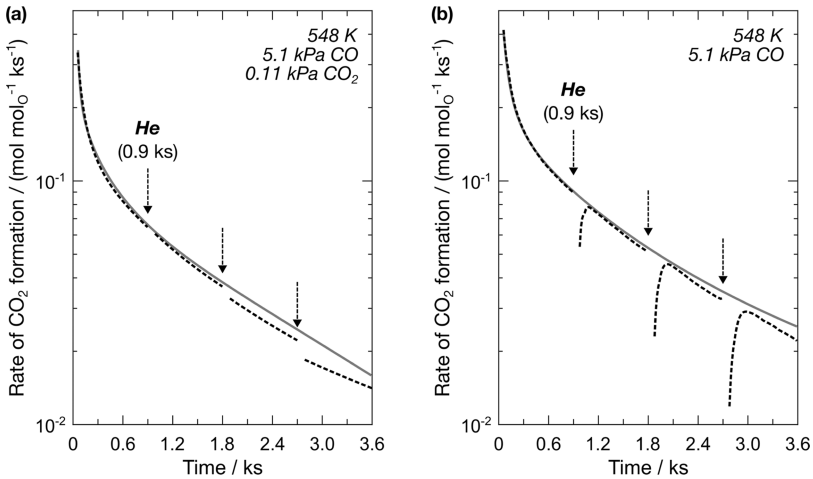


**Figure 5.** Rates of $CO_2$ formation (per removable O-atom) as a function of time for reactions of 5.1 kPa CO with $Ce_{0.5}Zr_{0.5}O_2$ (40 $m^2$ $g^{-1}$) at 548 K (a) with 0.11 kPa $CO_2$ and (b) without $CO_2$ added at the reactor inlet. The solid curves represent rates for reactions in which the inlet mixture was maintained without interruption for 3.6 ks, and the dashed curves represent those in which the inlet mixture alternated between CO (+ $CO_2$) for 0.9 ks and He for 0.9 ks. The down-pointing vertical arrows indicate the times when the reactor influent mixture was abruptly switched.

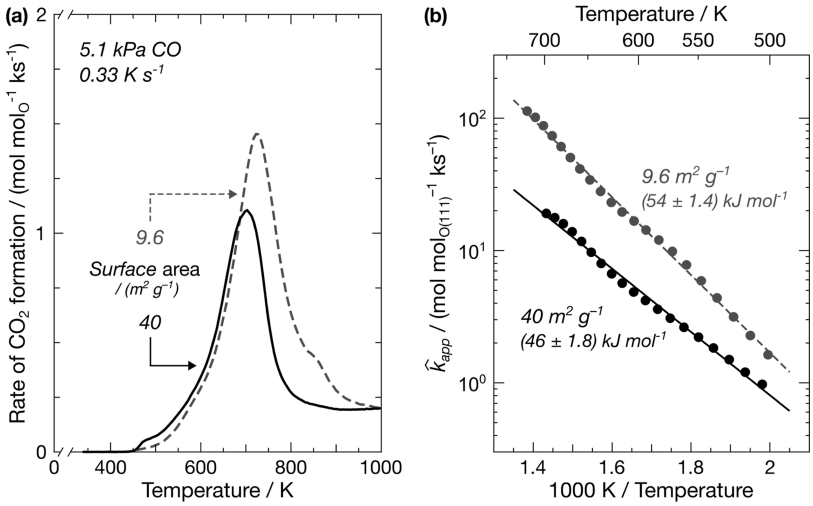


**Figure 6.** (a) Rates of $CO_2$ formation (per removable O-atom) as a function of temperature during temperature ramping (340−1000 K, 0.33 K $s^{-1}$) and (b) an Arrhenius plot of apparent first-order rate parameters (per removable O-atom on (111) surfaces; $\hat{k}_{app}$, eq 17) for reactions of 5.1 kPa CO with $Ce_{0.5}Zr_{0.5}O_2$ of 40 $m^2$ $g^{-1}$ (0.081 $mol_{O(111)}$ $mol_O^{-1}$; solid curve) and 9.6 $m^2$ $g^{-1}$ (0.020 $mol_{O(111)}$ $mol_O^{-1}$; dashed curve). The circles in (b) denote $\hat{k}_{app}$ values calculated from the measured rates in (a) using eq 17, and the lines in (b) represent those of best fit to the Arrhenius equation determined via linear regression.

increases monotonically with increasing $\lambda$ at all $\phi^2$ values (10 (solid), 3.2 (dashed), 1 (dash-dotted), 0.1 (dotted)) as $\lambda$ approaches and becomes larger than unity. For systems limited, in part, by lattice diffusion ($\phi^2 \geq 1$), a dwell duration that corresponds to $\lambda \geq 0.1$ leads to spatial gradients in $\mu_O$ that relax sufficiently to give rates that are detectably larger after the inert dwell period ($\chi \geq 1.2$); for diffusion-limited systems ($\phi^2 \gg 10$), even shorter dwells ($\lambda \geq 0.003$) led to higher rates ($\chi \geq 1.2$). Figure 4b shows that $\chi$ values are unity at all $\lambda$ values for $\phi^2$ values less than unity, irrespective of dwell time ($\lambda$) because spatial gradients are kinetically inconsequential during O-removal processes limited exclusively by surface reaction rates. Experiments analogous to those illustrated by this example (Figures 3 and 4) were performed to assess the extent to which significant intracrystal gradients in $\mu_O$ persist during CZO reduction by CO, thus informing as to whether lattice diffusion is kinetically relevant or not for O-atom removal rates.

Figure 5a shows O-removal rates (from rates of $CO_2$ formation) during experiments intended to mimic the illustrative examples (depicted in Figure 3) on CZO (40 $m^2$ $g^{-1}$) at 548 K. The gray curve shows these rates during contact with a stream of CO (as the reductant) and some $CO_2$ added to the inlet stream (to avoid large axial gradients in $CO_2$ concentration along the packed bed reactor; 5.1 kPa CO, 0.11 kPa $CO_2$) for 3.6 ks (without an intervening inert dwell). The dashed black data are obtained from a similar experiment but with 0.9 ks intervening dwell periods in He between reactions in CO (+ $CO_2$) for 0.9 ks; after each reintroduction of CO (+ $CO_2$), there is a brief hydrodynamic delay (∼40 s), as evidenced by the transient behavior of Ar, present as a tracer.

The data in Figure 5a show that O-removal rates are similar immediately before and after inert dwell periods, consistent with the absence of consequential gradients in O-atom chemical potential within CZO crystals and with lattice diffusion processes that are much faster than CO−$CO_2$


https://doi.org/10.1021/acs.jpcc.2c08117
J. Phys. Chem. C 2023, 127, 2936−2952

equilibration in surface reactions. The values of $\chi$ from these experiments are near unity (1.0, 0.94, and 0.91) at all extents of reduction ($\xi_{red}$ = 0.094, 0.13, and 0.16); these extents of reduction exceed those for the removal of one O-monolayer (0.081), a demonstration that $\phi^2$ values are much smaller than unity and that surface reaction of CO with surface O-atoms is the sole rate-limiting step in O-removal from CZO crystals at 548 K and $\xi_{red} \leq 0.16$.

An analogous experiment but with reaction and dwell durations of 3.6 ks (instead of 0.9 ks, as in Figure 5) and without $CO_2$ in the reactor inlet (instead of 0.11 kPa $CO_2$, as in Figure 5a) also gave a $\chi$ value near unity (1.0) at an extent of reduction of 0.30, showing that lattice diffusion remains kinetically irrelevant at $\xi_{red} \leq 0.30$. The results here together with the results in Figure 2, which show that O-atom removal rates with 0.52 kPa CO exceed those with 3.6 kPa $H_2$, indicate that CZO reduction by $H_2$ is also limited by surface reaction rates, since O-atom removal with $H_2$ is slower than O-atom removal with CO which is even slower still than lattice diffusion; thus, $\phi^2$ (eq 9) values for reduction by $H_2$ are less than those for reduction by CO which, in turn, are (much) less than unity. Hori et al.[50] performed similar types of experiments with 5 s (instead of 0.9 ks) reactions of 1 kPa (instead of 5.1 kPa) CO at 773 K (instead of 548 K) with $CeO_2$ (7.0 $m^2$ $g^{-1}$) and $Ce_{0.25}Zr_{0.75}O_2$ (7.7 $m^2$ $g^{-1}$; instead of $Ce_{0.5}Zr_{0.5}O_2$ (40 $m^2$ $g^{-1}$)) which gave $\chi$ values near unity upon reintroduction of CO after an inert ($N_2$) dwell period of 25 s. They concluded based on the absence of detectable increases in rates upon inert dwell periods that O-atom removal rates with CO are not limited by lattice diffusion, consistent with the results and conclusions of the present study.

The use of CO (5.1 kPa) without $CO_2$ added to the inlet stream (Figure 5b) at 548 K on $Ce_{0.5}Zr_{0.5}O_2$ (40 $m^2$ $g^{-1}$) also gives $\chi$ values near unity, but with an initial transient that reflects the replenishment of bound $CO_2$ that was removed during the inert dwell. The rates of $CO_2$ formation are always smaller when $CO_2$ (0.11 kPa) is added to the inlet stream (Figure 5a vs 5b), consistent with the inhibition of surface reaction rates by $CO_2$ as described in Section 3.1. The initial transients are absent near time zero when the CZO crystals are fully oxidized, suggesting that the inhibiting species are $CO_2$ molecules bound to surface anion vacancies.

The kinetic relevance of surface reactions for O-removal rates makes surface properties consequential. Figure 6a shows O-atom removal rates (per removable O-atom) with 5.1 kPa CO on $Ce_{0.5}Zr_{0.5}O_2$ with surface areas of 40 $m^2$ $g^{-1}$ (solid) and 9.6 $m^2$ $g^{-1}$ (dashed) as temperature increased (at 0.33 K $s^{-1}$) from 340 to 1000 K. The rates initially increase with increasing temperature before decreasing as O-atoms are consumed; they become less sensitive above 800 K, possibly because O-atom stability increases as CZO samples reduce.[10−12,20−23,28] The onset of $Ce_{0.5}Zr_{0.5}O_2$ reduction appears at 480 K on the sample with higher surface area and at 520 K for the other sample, a trend also observed for the temperatures required to achieve maximum rates (700 vs 720 K).

Such rate comparisons based on onset and maximum temperatures, however, do not allow for rigorous assessment of surface properties because, even at identical temperatures, the number of removable O-atoms remaining within the two different CZO samples are different. A more rigorous assessment requires that rates be normalized by the number of remaining removable O-atoms and that they be reported based on the number of removable O-atoms exposed on CZO surfaces. A comparison of apparent first-order rate parameters ($\hat{k}_{app}$, per removable O-atom exposed on CZO surfaces) enables such an assessment

$$\hat{k}_{app} = \frac{\hat{r}_{CO_2}(t)}{[O](t)} \tag{17}$$

where $\hat{r}_{CO_2}(t)$ and $[O](t)$ represent the $CO_2$ formation rate (per removable O-atom exposed on (111) surfaces of $Ce_{0.5}Zr_{0.5}O_2$) and the residual number of removable O-atoms within the CZO crystal at each time $t$, respectively. The latter is given by

$$[O](t) = 1 - \left(đ_{(111)} \int_0^t \hat{r}_{CO_2}(t')dt'\right) = 1 - \xi_{red}(t) \tag{18}$$

where $đ_{(111)}$ is the ratio of removable O-atoms exposed on (111) surfaces of $Ce_{0.5}Zr_{0.5}O_2$ to that within the entire $Ce_{0.5}Zr_{0.5}O_2$ crystal (0.081 and 0.020 for 40 and 9.6 $m^2$ $g^{-1}$, respectively). The term in parentheses in eq 18 is the extent of reduction ($\xi_{red}$).

Figure 6b shows $\hat{k}_{app}$ values for the two CZO samples, calculated from the rates in Figure 6a using eqs 17 and 18. The apparent first-order rate parameters (per removable O-atom exposed on CZO surfaces) are different at each temperature, indicating that the properties (and not just the surface area) of CZO surfaces influence surface reactions with CO. These rate constants increase exponentially with increasing temperature between the onset (ca. 500 K) and maximum (ca. 700 K) temperatures, during which $\xi_{red}$ values increase from 0 to about 0.30. These trends (linear in the semilogarithmic plots of $\hat{k}_{app}$ against reciprocal absolute temperature) correspond to apparent activation energies of 46 (±1.8) and 54 (±1.4) kJ $mol^{-1}$ for the 40 and 9.6 $m^2$ $g^{-1}$ samples, respectively. The surface properties that may account for such differences in $\hat{k}_{app}$ values and temperature effects include the identity and distribution of exposed crystal facets and the local arrangement of Ce and Zr cations at CZO surfaces. The next section describes the consequences of a deliberate and specific surface modification that demonstrates that surfaces matter and surface reactions limit O-atom removal rates on CZO.

**3.3. Consequences of Dispersing Pt Nanoparticles at CZO Surfaces for O-Removal Rates.** One such surface modification is ubiquitous in automotive exhaust practice; it entails the dispersion of Pt nanoparticles onto CZO surfaces. This additional surface function would introduce different rate parameters for surface reactions ($k_{red}$ and $f_{red}$, eq 7) and distinct kinetic trends with reactant or product concentrations ($f_{red}$, eq 7) than for metal-free CZO surfaces; this surface modification, if particularly competent for surface reactions and able to communicate with CZO surfaces, may increase $\phi^2$ values (eq 9), thus rendering lattice diffusion relevant in determining O-removal rates. In contrast, the functional form of diffusion flux (eq 3), the O-atom mobility ($\sigma_O$), or the relationship between chemical potential ($\mu_O$) and concentration of O-atoms ($C_O$) would not be altered upon atomic contact between Pt and CZO surfaces, which could only alter the driving force for diffusion ($-\nabla\mu_O$) by influencing the surface chemical potential of O-atoms set by surface reactions.

Figure 7 shows apparent first-order rate parameters ($\hat{k}_{app}$, eq 17) as the extent of reduction ($\xi_{red}$, eq 18) increases with time (5.1 kPa CO; 548 K) on CZO (40 $m^2$ $g^{-1}$; solid curve) and on Pt/CZO (1% wt; dashed curve). The filled symbols represent $\hat{k}_{app}$ values extrapolated to the time of initial contact with CO


https://doi.org/10.1021/acs.jpcc.2c08117
J. Phys. Chem. C 2023, 127, 2936−2952

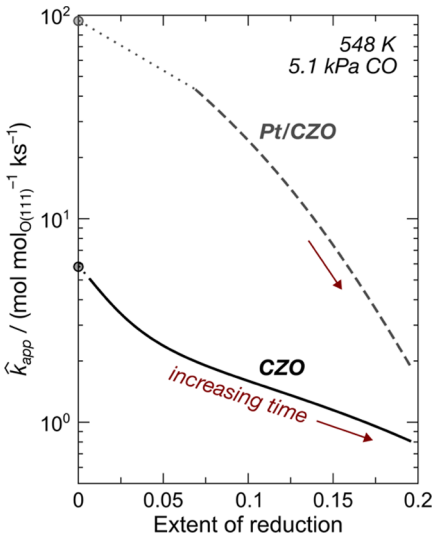


**Figure 7.** Apparent first-order rate parameters ($\hat{k}_{app}$, eq 17) as a function of extent of reduction ($\xi_{red}$, eq 18) for reactions of 5.1 kPa CO with $Ce_{0.5}Zr_{0.5}O_2$ (solid curve; 40 $m^2$ $g^{-1}$) and Pt/$Ce_{0.5}Zr_{0.5}O_2$ (dashed curve; 1% wt Pt) at 548 K. These $\hat{k}_{app}$ values were calculated from measured rate versus time data, and the dotted lines represent extrapolation of that data to zero time.

(from semilogarithmic plots of O-removal rates vs time). These $\hat{k}_{app}$ values are significantly larger for Pt/CZO than CZO at all values of $\xi_{red}$; such rate enhancements are well known when Pt, Pd, or Rh nanoparticles are dispersed on CZO surfaces.[14,16,17,50−53] These rate enhancements reflect O-atom removal from the bulk of CZO crystals; they cannot reflect the sole kinetic relevance of lattice diffusion because metal nanoparticles only influence surface properties and thus the relevant surface boundary condition in reaction-transport formalisms (eq 8). These data confirm that such surface properties are consequential for rates, but they could not influence rates when CO−$CO_2$ (or $H_2$−$H_2O$) interconversions are equilibrated at surfaces and lattice diffusion is the sole determinant of O-atom removal dynamics, a conclusion also reached from the experiments and mechanistic models in Sections 3.1 and 3.2.

The number of O-atoms removed may include some present in $PtO_2$ nanoparticles formed during $O_2$ treatment; these would contribute up to 0.06 O-atoms per removable O-atom in CZO (for 1% wt Pt/CZO). Thermodynamic calculations show that $PtO_2$ formation from Pt and $O_2$ at 548 K is feasible ($\Delta G_{548\ K} = -40$ kJ $mol^{-1}$).[54] Yet, $\hat{k}_{app}$ values remain about 10-fold larger when Pt nanoparticles are present at $\xi_{red}$ values well in excess of 0.06 (Figure 7), indicative of reactivity enhancements that reflect the removal of O-atoms from the surface and the bulk of CZO crystals.

The presence of Pt nanoparticles on CZO surfaces increases the rates of O-atom removal by providing an additional pathway that consumes O-atoms much faster than those prevalent on CZO surfaces. The reaction between a bound CO (CO···$Pt_s$) and an O-adatom (O···$Pt_s$) on Pt

$$CO\cdots Pt_s + O\cdots Pt_s \rightarrow CO_2 + 2\ Pt_s \tag{19}$$

must be faster than reactions between CO and an O-atom on the CZO surface ($O_s$)

$$CO + O_s \rightarrow CO_2 \tag{20}$$

since the apparent first-order rate parameter is larger at all extents of reduction for Pt/CZO than for CZO (Figure 7). This additional pathway provided by Pt (eq 19) becomes competent only because lattice diffusion is fast and rapidly replenishes O···$Pt_s$ species as they are consumed by CO. More specifically, fast lattice diffusion results in equilibration in O-atom chemical potential both between the surface and bulk ($O_b$) of CZO crystals

$$O_s \rightleftharpoons O_b \tag{21}$$

and between CZO crystals and Pt surfaces

$$O_b + Pt_s \rightleftharpoons O\cdots Pt_s \tag{22}$$

where $\rightleftharpoons$ denotes a quasi-equilibrated process. O···$Pt_s$ species react with CO (eq 19) but are rapidly restored by lattice diffusion (eqs 21 and 22), leading to higher O-removal rates but only for CZO crystals that contain Pt nanoparticles at their surfaces. The synthesis protocols used to form Pt (Section 2.1) may lead to their absence from some CZO crystals, such that the faster pathway for CZO reduction (eqs 19 and 22), enabled only upon atomic contact between Pt and CZO surfaces, is not accessible to every crystal. As a result, O-atom removal rates increase with increasing Pt amount before becoming insensitive to it once every CZO crystal is in contact with a Pt nanoparticle, as shown previously for Pt/CZO reduction by CO at 573 K.[50]

The values of $\hat{k}_{app}$ on Pt/CZO decreased more strongly as $\xi_{red}$ increased than on CZO (Figure 7), possibly as a result of distinct surface reaction rate equations for CZO and Pt/CZO, each parameterized with a distinct set of kinetic and thermodynamic parameters ($k_{red}$ and $f_{red}$, eq 7) that exhibit distinct functional dependencies on $\xi_{red}$. Rates of O-atom removal from CZO and Pt/CZO indeed show different trends with CO pressure (Figure S2; SI); the temperatures at which the maximum rate occurs during temperature ramping (340 to 1000 K, 0.33 K $s^{-1}$) decrease with increasing CO pressure for CZO reduction but remains unchanged for Pt/CZO, reflecting positive- and zero-order kinetics with respect to CO for CZO and Pt/CZO, respectively. It is also plausible that O-removal rates become limited, at least in part, by lattice diffusion as the presence of Pt nanoparticles increases surface reaction rates and CO−$CO_2$ (and $H_2$−$H_2O$) interconversion reactions at surfaces approach equilibrium.

Dwell experiments on Pt/CZO (1% wt) at 498 K (Figure 8; 5.1 kPa CO, 0.11 kPa $CO_2$) were performed analogously to those for CZO at 548 K (Figure 5a; 5.1 kPa CO, 0.11 kPa $CO_2$); these experiments (Figure 8) involved cycling between CO−$CO_2$ mixtures for 0.3 ks and then dwells in He for 0.9 ks. The number of O-atoms removed by the end of the first cycle corresponds to about two monolayers of removable O-atoms and therefore to the extraction of some O-atoms from the bulk of CZO crystals. The dotted curves represent linear extrapolations of semilogarithmic plots to early times after each switch between CO−$CO_2$ and He (data are affected initially because of hydrodynamic delays; ∼40 s). O-atom removal rates for Pt/CZO after 0.9 ks inert dwell periods ($\lambda$ = 0.04−0.2) were slightly higher than at the end of the preceding O-removal period ($\chi$ = 1.2−1.4), a finding that indicates some intervening relaxation of spatial gradients in oxygen chemical potential within CZO crystals at 498 K and for $\xi_{red}$ values between 0 and 0.25. These results contrast those of dwell experiments on CZO at 548 K (Figure 5) which gave negligible enhancement factors ($\chi$ = 0.9−1.0) after similar


https://doi.org/10.1021/acs.jpcc.2c08117
J. Phys. Chem. C 2023, 127, 2936−2952

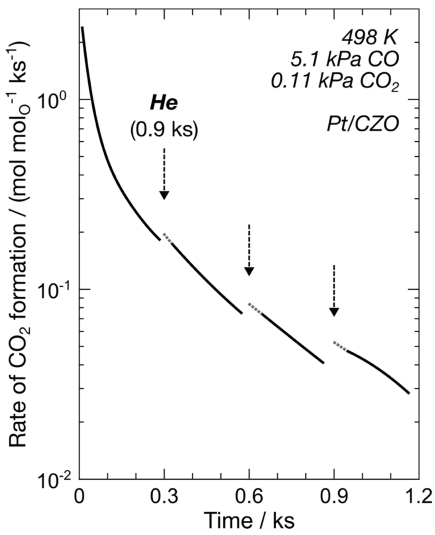


**Figure 8.** Rates of $CO_2$ formation (per removable O-atom) as a function of reaction time for reactions of 5.1 kPa CO + 0.11 kPa $CO_2$ with 1% wt Pt/$Ce_{0.5}Zr_{0.5}O_2$ (Pt/CZO) at 498 K. The solid curves represent rates for a reaction in which the inlet mixture was alternated between CO (+ $CO_2$) for 0.3 ks and He for 0.9 ks. The down-pointing vertical arrows indicate the reaction times when the reactor influent mixture was abruptly switched between CO (+ $CO_2$) and He. The dotted curves represent linear extrapolations in the semi-logarithmic plot to earlier times that are affected by the brief hydrodynamic delay (~40 s).

dwell durations ($\lambda$ = 0.02−0.1) for $\xi_{red} \leq 0.30$. Thus, the faster pathway for O-atom removal provided by Pt (eqs 19 and 22) increases surface reaction rates (and $\phi^2$ values, eq 9) to effect diffusional limitations.

The different O-removal rates at similar $CO_2$/CO ratios but different pressures of CO and $CO_2$ and for CO/$CO_2$ and $H_2$/$H_2O$ ratios that would give the same O-chemical potential (if surface reactions were equilibrated), taken together with small effects of inert dwell periods on O-removal rates from CZO and with the enhancements observed when Pt nanoparticles are dispersed on CZO surfaces, indicate that surface reactions are not at equilibrium and represent the sole kinetically relevant process for CZO reduction using CO and $H_2$ as reductants, without detectable contributions from lattice diffusion resistances. Such resistances do emerge, however, during O-removal from Pt/CZO because Pt nanoparticles dispersed on CZO surfaces increase surface reaction rates to render lattice diffusion kinetically relevant. In the next section, similar experimental protocols show that O-addition reactions occur at significantly lower temperatures than O-removal because surface reactions of oxidants ($O_2$, $N_2O$) are much faster, thus rendering O-addition limited by lattice diffusion at all conditions of practical interest.

**3.4. O-Atom Addition Rates on CZO and Effects of the Identity of the Oxidant ($O_2$, $N_2O$), Inert Dwell Periods, and Pt Nanoparticles.** The modeling approach and the equations derived for O-removal processes are unchanged when applied to O-addition (Section 2.3), except for the initial condition; this condition specifies a spatially uniform chemical potential within CZO crystals ($\mu_{O,0}$) that corresponds to stoichiometric $Ce_{0.5}Zr_{0.5}O_2$ (i.e., to $\xi_{red} = 0$) for O-removal. In contrast, O-addition reactions start with CZO samples that have been treated in $H_2$ (5.0 kPa) at 1000 K and annealed in He at 1000 K for a prescribed period of time to remove some O-atoms from the surface and bulk of CZO crystals (to $\xi_{red}$ values of 0.67 and 0.63 for the 40 and 9.6 $m^2$ $g^{-1}$ samples, respectively; $Ce_{0.5}Zr_{0.5}O_{1.83}$ and $Ce_{0.5}Zr_{0.5}O_{1.84}$) before exposure to an oxidant ($O_2$ or $N_2O$) at a target temperature. The initial condition for O-addition mole balances (eq 1) then becomes a spatially uniform chemical potential ($\mu_{O,0.67}$ or $\mu_{O,0.63}$) for the CZO samples (40 and 9.6 $m^2$ $g^{-1}$) at the extents of reduction imposed by the preceding thermal treatments (0.67 and 0.63). The description (Section 2.3) of the net volumetric rate of O-atom removal ($r_O^V$, eq 6) as a difference between CZO reduction and oxidation rates ($r_{red}^V - r_{ox}^V$) remains valid here, but $r_O^V$ is now negative for O-atom addition and can be, perhaps, more conveniently expressed in terms of the forward rate and approach-to-equilibrium for oxidation ($r_{ox}^V$ and $\eta_{ox}$)

$$-r_O^V = (r_{ox}^V - r_{red}^V) = r_{ox}^V(1 - \eta_{ox}) \tag{23}$$

The analogous nature of the physical and chemical processes for O-addition and O-removal renders the experimental strategies used to assess the kinetic relevance of lattice diffusion and surface reactions for O-removal (Sections 3.1−3.3) also suitable for O-addition processes.

O-atom addition reactions were initially performed with $O_2$, the relevant oxidant in automotive exhaust catalysis, solid oxide fuel cells, and chemical looping combustion, and at low temperatures (233 K) in attempts to avoid the very rapid $O_2$ consumption observed at higher temperatures and to measure rates in reactors without significant axial gradients in $O_2$ concentration.

The dashed curve in Figure 9 depicts the O-addition rates for $O_2$ (0.1 kPa) reactions with a pre-reduced CZO sample

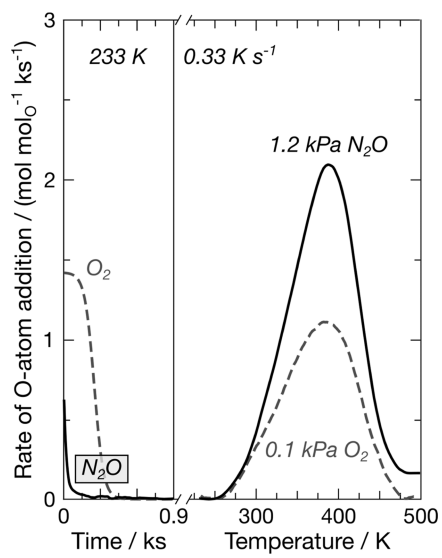


**Figure 9.** Rates of O-atom addition (per removable O-atom) versus time at 233 K for 0.9 ks and then versus temperature during temperature ramping (233−500 K, 0.33 K $s^{-1}$) for reactions of 1.2 kPa $N_2O$ (solid; $N_2$ formation rates) and 0.1 kPa $O_2$ (dashed; twice the $O_2$ consumption rates) with $Ce_{0.5}Zr_{0.5}O_{1.83}$ (40 $m^2$ $g^{-1}$).

($Ce_{0.5}Zr_{0.5}O_{1.83}$; $\xi_{red}$ = 0.67; 40 $m^2$ $g^{-1}$), first at a constant temperature (233 K for 0.9 ks; shown vs time in the left panel) and then as the temperature increased from 233 to 500 K at 0.33 K $s^{-1}$ (shown vs temperature in the right panel); the very initial rate at 233 K corresponds to complete $O_2$ conversion. At 233 K, 0.31 O-atoms are added per total removable O-atoms in


https://doi.org/10.1021/acs.jpcc.2c08117
J. Phys. Chem. C 2023, 127, 2936−2952

stoichiometric $Ce_{0.5}Zr_{0.5}O_2$ (Table 1; Experiment A, Step 1), and another 0.35 O-atoms per removable O-atom are then added to CZO during ramping to 500 K (Experiment A, Step 2). These combined uptakes are similar to those expected from complete reoxidation of the initial reduced CZO sample (0.67; Experiment A, Step 0), which converts $Ce_{0.5}Zr_{0.5}O_{1.83}$ fully to $Ce_{0.5}Zr_{0.5}O_2$ at rather mild conditions (0.1 kPa $O_2$; below 500 K). The temperature for the onset of $Ce_{0.5}Zr_{0.5}O_2$ reduction by CO (480 K; Figure 6A) is similar to that required to complete the reoxidation of $Ce_{0.5}Zr_{0.5}O_{1.83}$ by $O_2$ (480 K, Figure 9), indicating that O-atom addition by $O_2$ is much faster than the surface reaction for O-atom removal by CO.

**Table 1. Amounts of $O_2$ Consumed and $H_2O$ Formed and Values of Extent of Reduction in Various Reactions of $O_2$ and $H_2$ with $Ce_{0.5}Zr_{0.5}O_{2-x}$**

| expt | | step | 1/2 ($O_2$ cons.)[a] | $H_2O$ formed[b] | extent of reduction[c] |
|---|---|---|---|---|---|
| A | 0 | 5.0 kPa $H_2$<br>1000 K, 7.2 ks | – | 0.67 | 0.67 |
| A[d] | 1 | 0.1 kPa $O_2$<br>233 K, 0.9 ks | 0.31 | – | 0.36 |
| A[d] | 2 | 0.1 kPa $O_2$<br>233–500 K, 0.33 K $s^{-1}$ | 0.35 | – | 0.01 |
| B | 0 | 5.0 kPa $H_2$<br>1000 K, 7.2 ks | – | 0.67 | 0.67 |
| B | 1 | 0.1 kPa $O_2$<br>233 K, 0.9 ks | 0.31 | – | 0.36 |
| B | 2 | He<br>233–500 K, 0.33 K $s^{-1}$ | 0 | 0 | 0.36 |
| B | 3 | 5.0 kPa $H_2$<br>1000 K, 7.2 ks | – | 0.32 | 0.68 |

[a]Dimensions of O-atom added per total removable O in $Ce_{0.5}Zr_{0.5}O_2$. [b]Dimensions of O-atom removed per total removable O in $Ce_{0.5}Zr_{0.5}O_2$. [c]Equivalent to extent of reaction for $Ce_{0.5}^{IV}Zr_{0.5}O_2 \rightarrow 0.25O + Ce_{0.5}^{III}Zr_{0.5}O_{1.75}$. [d]Figure 9 shows the rates of O-atom addition versus time and temperature for Steps 1 and 2, respectively, of Experiment A.

Some of the O-atoms added may be present as bound $O_2$ species without dissociation at 233 K, as evident from vibrational and spin resonance spectral features for superoxo and peroxo species detected upon contact of partially reduced CZO (and $CeO_2$) with $O_2$ at subambient temperatures;[55−61] these features persisted to 500 K in contact with $O_2$[57] and to 450 K in its absence.[60]

The number of O-atoms consumed at 233 K (Table 1; Experiment A, Step 1) corresponds to 1.7, 2.1, or 2.9 $O_2$ molecules per surface vacancy if CZO crystal surfaces exposed exclusively a (111), (110), or (100) facet, respectively (calculated based on 40 $m^2$ $g^{-1}$, 0.52909 nm lattice constant, and an extent of reduction of 0.67). These binding stoichiometries are similar to those for the binding of two $O_2$ molecules at each vacancy, as required for the formation of superoxo species. The presence of such species may render conclusions about the extent of O-atom incorporation into CZO crystals equivocal.

Subsequent heating of a reduced CZO sample exposed to 0.1 kPa $O_2$ (at 233 K for 0.9 ks) to 500 K in a He stream (Table 1; Experiment B, Step 2) did not lead to detectable $O_2$ evolution, suggesting that bound $O_2$ (superoxo) species formed at 233 K either persisted on the CZO surface at 500 K, in contrast with the spectroscopic evidence,[57,60] or dissociated, with O-atoms formed diffusing into the bulk of CZO during temperature ramping in He. A subsequent treatment in $H_2$ (5.0 kPa $H_2$; 1000 K; Experiment B, Step 3) led to the evolution of 0.32 $H_2O$ molecules (per total removable O-atom in $Ce_{0.5}Zr_{0.5}O_2$), thus completing an O-atom balance and confirming that all of the $O_2$ consumed in Step 1 was indeed retained as $O_2$ or as O-atoms on or within the pre-reduced CZO.

$N_2O$ oxidants circumvent these concerns regarding bound dioxygen species and allow O-addition rates to be measured directly from $N_2$ formation rates (instead of $O_2$ consumption) without stoichiometric ambiguities. Figure 9 shows O-addition rates using $N_2O$ (1.2 kPa; solid curves) using the same pre-

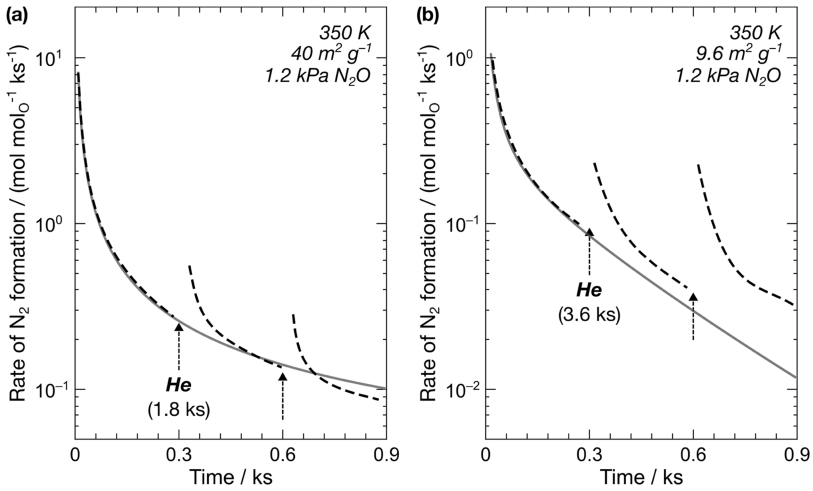


**Figure 10.** Rates of $N_2$ formation (per removable O-atom) as a function of reaction time for reactions of 1.2 kPa $N_2O$ at 350 K with (a) $Ce_{0.5}Zr_{0.5}O_{1.83}$ (40 $m^2$ $g^{-1}$) and (b) $Ce_{0.5}Zr_{0.5}O_{1.84}$ (9.6 $m^2$ $g^{-1}$). The solid gray curves represent rates for reactions in which the inlet mixture was maintained at the specified conditions without interruption for 0.9 ks, and the dashed black curves represent those in which the inlet mixture alternated between $N_2O$ for 0.3 ks and He for (a) 1.8 ks or (b) 3.6 ks. The up-pointing vertical arrows indicate the times when the reactor influent mixture was abruptly switched between $N_2O$ and He.


https://doi.org/10.1021/acs.jpcc.2c08117
J. Phys. Chem. C 2023, 127, 2936−2952

reduced CZO sample ($Ce_{0.5}Zr_{0.5}O_{1.83}$; $\xi_{red}$ = 0.67; 40 $m^2$ $g^{-1}$) and temperature protocols as with $O_2$ oxidants (Figure 9, dashed curves). The number of O-atoms added at 233 K was small with $N_2O$ as the oxidant (~0.02 O-atoms per total removable O-atoms in $Ce_{0.5}Zr_{0.5}O_2$); $N_2$ evolved between 250 and 500 K without any detectable concurrent formation of $O_2$, which ultimately formed along with $N_2$ in stoichiometric amounts only above 700 K via its stoichiometric decomposition (on CZO surfaces). The combined amounts of $N_2$ formed during this experiment correspond to 0.69 O-atoms per removable O-atom, consistent with the reoxidation of $Ce_{0.5}Zr_{0.5}O_{1.83}$ ($\xi_{red}$ = 0.67) to stoichiometric $Ce_{0.5}Zr_{0.5}O_2$.

The onset temperature for detectable O-atom addition to $Ce_{0.5}Zr_{0.5}O_{1.83}$ (40 $m^2$ $g^{-1}$) is similar for 0.1 kPa $O_2$ and 1.2 kPa $N_2O$ (250 K), and the maximum in rates also occur at similar temperatures (380 vs 390 K). Such similarities would represent an implausible coincidence if O-addition rates were limited by the surface reactions for these two different oxidants. The similar features in Figure 9 suggest instead that the rates of O-atom addition by $O_2$ and $N_2O$ reflect the rates of lattice diffusion, the functional form of which (eq 3) has no explicit dependence on oxidant identity or concentration.

These speculations can be probed with inert dwell protocols for $N_2O$ reactions that parallel those used for O-removal by CO (Section 3.2, Figure 5). The solid curve in Figure 10a shows O-addition rates (1.2 kPa $N_2O$) to pre-reduced CZO ($Ce_{0.5}Zr_{0.5}O_{1.83}$; 40 $m^2$ $g^{-1}$) at 350 K for a continuous period of 0.9 ks, and the dashed curves show O-addition rates when exposure to $N_2O$ (1.2 kPa; 0.3 ks) was sequentially interrupted by contact with He for 1.8 ks. O-addition rates (350 K; Figure 10) were higher after a He dwell than at the end of the preceding $N_2O$ reaction, in contrast to the findings for O-removal processes using CO (548 K; Figure 5), which were essentially unaffected by intervening inert dwells. These data indicate that spatial gradients in O-atom chemical potential are present during the oxidation of partially reduced CZO crystals, presumably a consequence of the fast (and thermodynamically favorable) activation of oxidants at CZO crystal surfaces (also evident from O-addition reactions that require significantly lower temperatures than O-removal). The rate enhancements observed after inert dwell periods ($\chi$, Figure 3) are 2.4 and 2.2 at extents of reduction ($\xi_{red}$) of 0.43 and 0.38, and the corresponding dimensionless dwell durations ($\lambda$, Figure 3) are 0.4 and 0.2. These values of $\chi$ and $\lambda$ are consistent with $\phi^2$ (eq 9) values of about 10 when considered in the context of the illustrative examples described in Section 3.2 (Figure 4), with O-addition from $N_2O$ oxidants being significantly limited by lattice diffusion at 350 K and values of $\xi_{red}$ between 0.38 and 0.43, and with the presence of kinetically consequential spatial gradients in oxygen chemical potential during CZO oxidation.

These conclusions lead to the expectation that the size of CZO crystals (but not their surface properties) would influence O-addition rates. An analogous inert dwell experiment (Figure 10b) on another CZO sample ($\xi_{red}$ = 0.63, $Ce_{0.5}Zr_{0.5}O_{1.84}$) but with lower surface area (9.6 vs 40 $m^2$ $g^{-1}$) also led to rate enhancements. The enhancements were larger for the larger crystals with lower surface area ($\chi$ = 2.9 and 5.6; Figure 10b; 9.6 $m^2$ $g^{-1}$) compared to those for the smaller crystals ($\chi$ = 2.4 and 2.2; Figure 10a; 40 $m^2$ $g^{-1}$), even though the larger CZO crystals were subjected to shorter dwell durations ($\lambda$ < 0.3 and $\lambda$ < 0.4 for, respectively, 9.6 and 40 $m^2$ $g^{-1}$). These trends in $\chi$ and $\lambda$ values reflect $\phi^2$ values that are larger for the larger crystals, consistent with expectations from the reaction-transport formalisms (Section 2.3) which show that diffusional limitations, as quantified by $\phi^2$ (eq 9), increase quadratically with increasing crystal size ($R_p$).

A ratio of diffusive flux ($J_O$; eq 3) values for two samples with different crystal sizes ($J_{O,1}/J_{O,2}$) is equal to the inverse ratio of their sizes ($R_{p,2}/R_{p,1}$) but only when compared at conditions that result in similar O-atom concentrations ($C_O$) and nondimensional spatial gradients in O-atom chemical potential ($\partial\hat{\mu}_O/\partial\hat{r}$). Figure 11 shows areal rates of O-atom addition (as $N_2$ formation rates) versus time for reactions of $N_2O$ (1.2 kPa) at 350 K with $Ce_{0.5}Zr_{0.5}O_{1.83}$ (40 $m^2$ $g^{-1}$; solid) and with $Ce_{0.5}Zr_{0.5}O_{1.84}$ (9.6 $m^2$ $g^{-1}$; dashed). These areal rates reflect diffusive fluxes only at times after that required to form a monolayer of O-atoms; before surfaces reach saturation, they reflect, at least in part, surface reaction rates. The areal O-atom addition rates for the two samples (40 $m^2$ $g^{-1}$ (solid) and 9.6 $m^2$ $g^{-1}$ (dashed); Figure 11) are coincident at early times, consistent with these rates initially reflecting those for the surface reaction between $N_2O$ and surface anion vacancies. The dotted curves in the inset of Figure 11 represent estimates of diffusion rates at early times that were determined from linear regressions of rate versus time data in the semilogarithmic plots at times just after reaching surface saturation (corresponding to 0.054 and 0.013 of $N_2$ formed per total removable O-atom for the 40 $m^2$ $g^{-1}$ ($\xi_{red}$ = 0.67) and 9.6 $m^2$ $g^{-1}$ ($\xi_{red}$ = 0.63) samples, respectively). The ratio of such rates when extrapolated to the times of initial contact (denoted by the circles in the inset of Figure 11) then corresponds to a comparison at similar values of $C_O$ (corresponding to saturation coverages) and $\partial\hat{\mu}_O/\partial\hat{r}$ (corresponding to gradients at times of initial contact). This estimate of diffusive flux is about three times higher for the smaller particles (40 $m^2$ $g^{-1}$) than for the larger ones (9.6 $m^2$ $g^{-1}$), and this factor of three is in reasonable agreement with the inverse ratio of crystal sizes

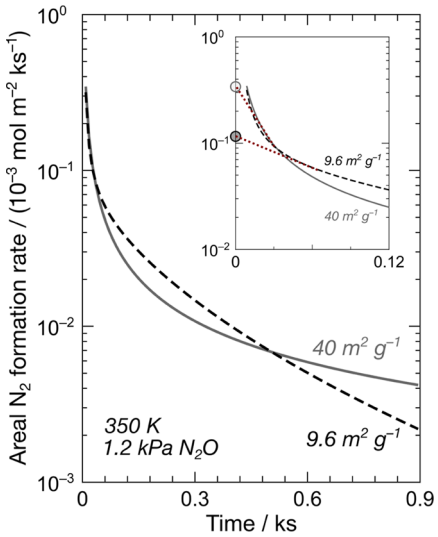


**Figure 11.** Rates of $N_2$ formation per surface area as a function of time for reactions of 1.2 kPa $N_2O$ with $Ce_{0.5}Zr_{0.5}O_{1.83}$ (40 $m^2$ $g^{-1}$; solid) and with $Ce_{0.5}Zr_{0.5}O_{1.84}$ (9.6 $m^2$ $g^{-1}$; dashed) at 350 K. The inset shows data at early times. The dotted curves are linear extrapolations in the semilogarithmic plots determined via linear regression of data at times immediately after that required for the addition of one O-monolayer; the circles at time zero then represent estimates of diffusive flux at saturation coverage of O-atoms.


https://doi.org/10.1021/acs.jpcc.2c08117
J. Phys. Chem. C 2023, 127, 2936−2952

of four (as estimated from the ratio of surface areas), consistent with the expectation that diffusive flux is inversely proportional to crystal size (eq 3).

The limiting nature of lattice diffusion processes is expected to lead to O-addition rates that are insensitive to the presence of Pt nanoparticles at CZO surfaces because such a surface modification would not affect the bulk transport ($\sigma_O$) and thermodynamic ($\gamma_O$) properties that influence diffusion flux (eqs 3 and 4). Figure 12 shows O-addition rates for $N_2O$ (1.2 kPa) reactions with partially reduced CZO ($Ce_{0.5}Zr_{0.5}O_{1.83}$; solid curve) and with the same sample but with Pt nanoparticles dispersed on CZO surfaces before reductive treatments (1% wt Pt; dashed curve) during temperature ramping from 233 to 500 K (0.33 K $s^{-1}$). As in the case of the similar traces for $N_2O$ vs $O_2$ reactions with $Ce_{0.5}Zr_{0.5}O_{1.83}$ (Figure 9), the onset temperature of $N_2$ formation (250 vs 250 K) and that for the maximum in rates (390 vs 380 K) were similar for CZO and Pt/CZO samples (Figure 12). The absence of detectable consequences of atomic contact between Pt and CZO surfaces, evident from the data in Figure 12, confirms that surface reactions do not influence O-addition rates and that, in contrast with the conclusions for O-removal rates using CO or $H_2$, lattice diffusion is the predominant resistance to O-addition from $N_2O$ or $O_2$. These diffusion rates reflect the thermodynamics and anion mobility of CZO crystals (eq 3), which are not influenced by the presence of Pt nanoparticles at their surfaces, while the rates of O-atom removal reflect the thermodynamic and kinetic parameters of surface reaction rate equations (eq 7).

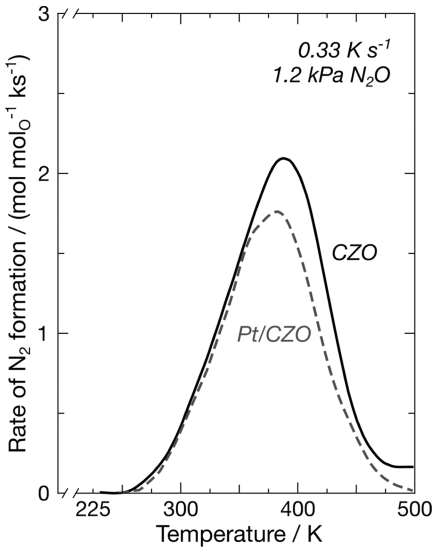


**Figure 12.** Rates of $N_2$ formation (per total removable oxygen) as a function of temperature during temperature ramping (233−500 K, 0.33 K $s^{-1}$) for the reaction of 1.2 kPa $N_2O$ with reduced CZO ($Ce_{0.5}Zr_{0.5}O_{1.83}$ (40 $m^2$ $g^{-1}$); solid curve) and reduced Pt/CZO (1% wt Pt/$Ce_{0.5}Zr_{0.5}O_{1.83}$; dashed curve).

Figure 13 shows a comparison between surface reaction rates during O-atom removal and lattice diffusion rates during O-atom addition. The solid curve represents apparent first-order rate parameters per removable O-atom for the reaction of CO (5.1 kPa) at 600 K with $Ce_{0.5}Zr_{0.5}O_2$ (40 $m^2$ $g^{-1}$; $k_{app}^{red}$) and the dashed curve for the reaction of $N_2O$ (1.2 kPa) at 350 K with $Ce_{0.5}Zr_{0.5}O_{1.83}$ (40 $m^2$ $g^{-1}$; $k_{app}^{ox}$). The $k_{app}^{red}$ and $k_{app}^{ox}$ values were calculated using the following equations analogous to $\hat{k}_{app}$ (eq 17; Figures 6b and 7)

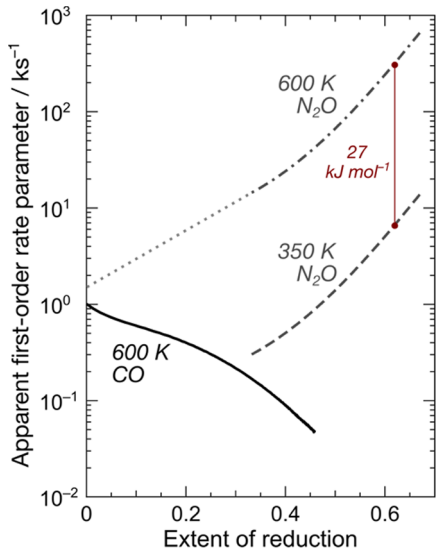


**Figure 13.** Apparent first-order rate parameters (eqs 24 and 25) versus extent of reduction ($\xi_{red}$) for the reaction of 5.1 kPa CO at 600 K with $Ce_{0.5}Zr_{0.5}O_2$ (40 $m^2$ $g^{-1}$; $\xi_{red}$ = 0; solid) and for the reaction of 1.2 kPa $N_2O$ at 350 K with $Ce_{0.5}Zr_{0.5}O_{1.83}$ (40 $m^2$ $g^{-1}$; $\xi_{red}$ = 0.67; dashed). The values for the dash-dotted curve for the reaction of 1.2 kPa $N_2O$ at 600 K with $Ce_{0.5}Zr_{0.5}O_{1.83}$ (40 $m^2$ $g^{-1}$; $\xi_{red}$ = 0.67) were calculated by extrapolating rate parameters in the dashed curve (350 K) using an activation barrier of 27 kJ $mol^{-1}$ at all extents of reduction. The dotted line is a linear extrapolation in the semilogarithmic plot of values in the dash-dotted curve.

$$k_{app}^{red} = \frac{r_{CO_2}(t)}{1 - \xi_{red}(t)} \tag{24}$$

$$k_{app}^{ox} = \frac{r_{N_2}(t)}{\xi_{red}(t)} \tag{25}$$

where $r_{CO_2}(t)$ and $r_{N_2}(t)$ are the rates, per removable O-atom, of $CO_2$ formation during reduction by CO and $N_2$ formation during oxidation by $N_2O$, respectively, at time $t$. The $k_{app}^{ox}$ values for O-atom addition at 350 K exceed the $k_{app}^{red}$ values for O-atom removal at 600 K when compared at identical extents of reduction, showing that rates of lattice diffusion during oxidation by $N_2O$ at 350 K exceed the rates of surface reaction during reduction by CO at 600 K at $\xi_{red}$ values between 0.32 and 0.46. Apparent activation barriers for O-atom addition by $N_2O$ were estimated to be between 27 and 62 kJ $mol^{-1}$ using the rate versus temperature data in Figure 9 and analysis identical to that described in Section 3.2 and depicted in Figure 6 for $\hat{k}_{app}$ (eq 17); then, $k_{app}^{ox}$ values at 350 K (Figure 13, dashed) were extrapolated to 600 K (Figure 13, dash-dotted) using the conservative estimate of 27 kJ $mol^{-1}$ for the Arrhenius temperature dependence. These $k_{app}^{ox}$ values at 600 K, and those estimated via linear extrapolation in the semilogarithmic plot to $\xi_{red}$ values not accessed in the O-addition experiments at 350 K (dotted; $\xi_{red}$ < 0.32), exceed the $k_{app}^{red}$ values at 600 K for all extents of reduction between 0 and 0.67. These results show that CZO oxidation is faster than CZO reduction, consistent with the previous conclusions that the former is limited by lattice diffusion while the latter is limited by surface reaction.


https://doi.org/10.1021/acs.jpcc.2c08117
J. Phys. Chem. C 2023, 127, 2936−2952

The effects of reactant identity ($O_2$ vs $N_2O$, Figure 9), inert dwell periods (Figure 10), CZO crystal size (Figure 11), and Pt nanoparticles (Figure 12) on O-addition rates to partially reduced CZO contrast those evident during O-removal from stoichiometric CZO (Figures 2, 5, 6, and 7, respectively). This discrepancy in the kinetic relevance of lattice diffusion between O-atom addition and removal cannot be ascribed to differences in the extents of reduction accessed in the oxidation and reduction experiments, since CZO oxidation rates by $N_2O$ and $O_2$ always exceed those for reduction by CO and $H_2$ (Figure 13). These experimental probes are all consistent with O-atom addition and removal being, respectively, diffusion- and reaction-limited for oxidants ($O_2$), reductants (CO and $H_2$), and conditions relevant to the practical deployment of CZO in automotive exhaust catalysis. They provide a systematic strategy for the analysis of processes involving surface reactions and lattice diffusion in chemical looping, oxidation−reduction cycles for thermochemical energy storage−release, and selective oxidations and reductions of substrates using lattice O-anions and anion vacancies.

## 4. CONCLUSIONS

This report details the methodology and reaction-transport formalisms for experiments designed to probe whether reduction and oxidation rates of reducible oxides are limited by surface reactions or lattice diffusion and describes the results of their application to ceria-zirconia (CZO) solid solutions. CZO reduction rates with different reductant (CO) and oxidant ($CO_2$) concentrations and with different reductant and oxidant identities (CO and $CO_2$ vs $H_2$ and $H_2O$) do not coincide when compared at specific conditions that would have resulted in identical rates if the surface reactions were quasi-equilibrated, showing that reduction rates do not solely reflect lattice diffusion. In contrast, a comparison of CZO oxidation rates by $O_2$ and $N_2O$ suggests that these rates are limited by lattice diffusion, but the formation of surface-bound superoxo species during $O_2$ reactions renders this probe an imprecise adjudicator of the kinetic irrelevance of surface reactions for CZO oxidation. Experiments that reveal the magnitude of spatial gradients in oxygen chemical potential within CZO crystals during reaction show that such gradients are kinetically insignificant during O-atom removal but significant for O-atom addition, demonstrating that CZO reduction rates reflect solely surface reactions and that CZO oxidation experiences diffusional limitations. A comparison of CZO reduction rates between samples with 4-fold difference in surface area shows that surface properties beyond exposed area affect rates on CZO surfaces. Dispersing Pt nanoparticles on CZO surfaces increases rates of O-atom removal but did not affect those for O-atom addition, consistent with the former reflecting surface reaction rates and the latter lattice diffusion, since such modification to CZO surfaces only affects surface reaction rates. The fast lattice diffusion during reduction of Pt/CZO results in equivalent oxygen chemical potentials between oxide crystals and metal nanoparticles, and the rapid consumption of O-adatoms on Pt, versus the comparatively slow O-removal from CZO surfaces, enables Pt, when in atomic contact with CZO, to serve as a sink for O-atoms and a "porthole" for their removal. The results of these probe experiments together show that reduction and oxidation of CZO, by reductants (CO and $H_2$) and oxidants ($O_2$) relevant to its deployment as an oxygen "buffer" in automotive catalysis, are limited by rates of surface reactions and lattice diffusion, respectively. These results also exemplify the efficacy of the described experiments and formalisms to establish the kinetic relevance of reaction and diffusion for the half-cycle dynamics of reducing and oxidizing redox-active oxides.

## ■ ASSOCIATED CONTENT

### Supporting Information

The Supporting Information is available free of charge at https://pubs.acs.org/doi/10.1021/acs.jpcc.2c08117.

X-ray diffraction patterns and Raman spectra for the ceria-zirconia samples; profiles of oxygen removal rate versus temperature for reactions of CO (0.10, 0.49, and 5.1 kPa) on $Ce_{0.5}Zr_{0.5}O_2$ (120 $m^2$ $g^{-1}$) and Pt/$Ce_{0.5}Zr_{0.5}O_2$ (1% wt Pt, 120 $m^2$ $g^{-1}$) as the temperature was ramped from 340 to 1000 K at 0.33 K $s^{-1}$ (PDF)

## ■ AUTHOR INFORMATION


### Corresponding Author

**Enrique Iglesia** − *Department of Chemical and Biomolecular Engineering, University of California, Berkeley, Berkeley, California 94720, United States;* orcid.org/0000-0003-4109-1001; Email: iglesia@berkeley.edu

### Authors

**Andrew Hwang** − *Department of Chemical and Biomolecular Engineering, University of California, Berkeley, Berkeley, California 94720, United States*

**Jason Wu** − *Research and Advanced Engineering, Ford Motor Company, Dearborn, Michigan 48124, United States;* Present Address: Honeywell UOP, Des Plaines, Illinois 60017, United States

**Andrew "Bean" Getsoian** − *Research and Advanced Engineering, Ford Motor Company, Dearborn, Michigan 48124, United States;* orcid.org/0000-0003-1534-3818

Complete contact information is available at: https://pubs.acs.org/10.1021/acs.jpcc.2c08117


### Notes

The authors declare no competing financial interest.

While this article is believed to contain correct information, Ford Motor Company (Ford) does not expressly or impliedly warrant, nor assume any responsibility, for the accuracy, completeness, or usefulness of any information, apparatus, product, or process disclosed, nor represent that its use would not infringe the rights of third parties. Reference to any commercial product or process does not constitute its endorsement. This article does not provide financial, safety, medical, consumer product, or public policy advice or recommendation. Readers should independently replicate all experiments, calculations, and results. The views and opinions expressed are of the authors and do not necessarily reflect those of Ford. This disclaimer may not be removed, altered, superseded, or modified without prior Ford permission.

## ■ ACKNOWLEDGMENTS

This study was financially supported by the Ford Motor Company and the Vermeulen Chair endowment fund. The authors thank Dr. Gregory L. Tate for carefully proofreading this manuscript.

## REFERENCES


(1) Mars, P.; van Krevelen, D. W. Oxidations Carried Out by Means of Vanadium Oxide Catalysts. *Chem. Eng. Sci.* **1954**, *3*, 41−59.

(2) Ganduglia-Pirovano, M. V.; Hofmann, A.; Sauer, J. Oxygen Vacancies in Transition Metal and Rare Earth Oxides: Current State of Understanding and Remaining Challenges. *Surf. Sci. Rep.* **2007**, *62*, 219−270.

(3) McFarland, E. W.; Metiu, H. Catalysis by Doped Oxides. *Chem. Rev.* **2013**, *113*, 4391−4427.

(4) D'Souza, L. Thermochemical Hydrogen Production from Water using Reducible Oxide Materials: A Critical Review. *Mater. Renewable Sustainable Energy* **2013**, *2*, No. 7.

(5) van Santen, R. A.; Tranca, I.; Hensen, E. J. M. Theory of Surface Chemistry and Reactivity of Reducible Oxides. *Catal. Today* **2015**, *244*, 63−83.

(6) Zeng, L.; Cheng, Z.; Fan, J. A.; Fan, L.-S.; Gong, J. Metal Oxide Redox Chemistry for Chemical Looping Processes. *Nat. Rev. Chem.* **2018**, *2*, 349−364.

(7) Tuller, H. L.; Bishop, S. R. Point Defects in Oxides: Tailoring Materials Through Defect Engineering. *Annu. Rev. Mater. Res.* **2011**, *41*, 369−398.

(8) Steele, B. C. H.; Floyd, J. M. Oxygen Self-Diffusion and Electrical Transport Properties of Nonstoichiometric Ceria and Ceria Solid Solutions. *Proc. Br. Ceram. Soc.* **1971**, *19*, 55−76.

(9) Tuller, H. L.; Nowick, A. S. Doped Ceria as a Solid Oxide Electrolyte. *J. Electrochem. Soc.* **1975**, *122*, 255−259.

(10) Inaba, H.; Tagawa, H. Ceria-Based Solid Electrolytes. *Solid State Ionics* **1996**, *83*, 1−16.

(11) Chiodelli, G.; Flor, G.; Scagliotti, M. Electrical Properties of the $ZrO_2$-$CeO_2$ System. *Solid State Ionics* **1996**, *91*, 109−121.

(12) Mogensen, M.; Sammes, N. M.; Tompsett, G. A. Physical, Chemical and Electrochemical Properties of Pure and Doped Ceria. *Solid State Ionics* **2000**, *129*, 63−94.

(13) Steele, B. C. H. Materials for IT-SOFC Stacks: 35 Years R&D: The Inevitability of Gradualness? *Solid State Ionics* **2000**, *134*, 3−20.

(14) Yao, H. C.; Yao, Y. F. Y. Ceria in Automotive Exhaust Catalysts: I. Oxygen Storage. *J. Catal.* **1984**, *86*, 254−265.

(15) Trovarelli, A. Catalytic Properties of Ceria and $CeO_2$-Containing Materials. *Catal. Rev.* **1996**, *38*, 439−520.

(16) Kašpar, J.; Fornasiero, P.; Graziani, M. Use of $CeO_2$-Based Oxides in the Three-Way Catalysis. *Catal. Today* **1999**, *50*, 285−298.

(17) Jen, H.-W.; Graham, G. W.; Chun, W.; McCabe, R. W.; Cuif, J.-P.; Deutsch, S. E.; Touret, O. Characterization of Model Automotive Exhaust Catalysts: Pd on Ceria and Ceria−Zirconia Supports. *Catal. Today* **1999**, *50*, 309−328.

(18) Mullins, D. R. The Surface Chemistry of Cerium Oxide. *Surf. Sci. Rep.* **2015**, *70*, 42−85.

(19) Wu, J.; O'Neill, A. E.; Li, C.-H.; Jinschek, J. R.; Cavataio, G. Superior TWC Activity of Rh Supported on Pyrochlore-Phase Ceria Zirconia. *Appl. Catal., B* **2021**, *280*, No. 119450.

(20) Kim, T.; Vohs, J. M.; Gorte, R. J. Thermodynamic Investigation of the Redox Properties of Ceria−Zirconia Solid Solutions. *Ind. Eng. Chem. Res.* **2006**, *45*, 5561−5565.

(21) Zhou, G.; Shah, P. R.; Kim, T.; Fornasiero, P.; Gorte, R. J. Oxidation Entropies and Enthalpies of Ceria−Zirconia Solid Solutions. *Catal. Today* **2007**, *123*, 86−93.

(22) Boaro, M.; Desinan, S.; Abate, C.; Ferluga, M.; de Leitenburg, C.; Trovarelli, A. Study on Redox, Structural and Electrical Properties of $Ce_xZr_{1-x}O_2$ for Applications in SOFC Anodes. *J. Electrochem. Soc.* **2011**, *158*, P22−P29.

(23) Kuhn, M.; Bishop, S. R.; Rupp, J. L. M.; Tuller, H. L. Structural Characterization and Oxygen Nonstoichiometry of Ceria-Zirconia ($Ce_{1-x}Zr_xO_{2-\delta}$) Solid Solutions. *Acta Mater.* **2013**, *61*, 4277−4288.

(24) Nagai, Y.; Yamamoto, T.; Tanaka, T.; Yoshida, S.; Nonaka, T.; Okamoto, T.; Suda, A.; Sugiura, M. X-ray Absorption Fine Structure Analysis of Local Structure of $CeO_2$−$ZrO_2$ Mixed Oxides with the Same Composition Ratio (Ce/Zr = 1). *Catal. Today* **2002**, *74*, 225−234.

(25) Mamontov, E.; Egami, T.; Brezny, R.; Koranne, M.; Tyagi, S. Lattice Defects and Oxygen Storage Capacity of Nanocrystalline Ceria and Ceria-Zirconia. *J. Phys. Chem. B* **2000**, *104*, 11110−11116.

(26) Wang, R.; Crozier, P. A.; Sharma, R.; Adams, J. B. Measuring the Redox Activity of Individual Catalytic Nanoparticles in Cerium-Based Oxides. *Nano Lett.* **2008**, *8*, 962−967.

(27) Paier, J.; Penschke, C.; Sauer, J. Oxygen Defects and Surface Chemistry of Ceria: Quantum Chemical Studies Compared to Experiment. *Chem. Rev.* **2013**, *113*, 3949−3985.

(28) Rink, J.; Meister, N.; Herbst, F.; Votsmeier, M. Oxygen Storage in Three-Way-Catalysts is an Equilibrium Controlled Process: Experimental Investigation of the Redox Thermodynamics. *Appl. Catal., B* **2017**, *206*, 104−114.

(29) Koohi-Fayegh, S.; Rosen, M. A. A Review of Energy Storage Types, Applications and Recent Developments. *J. Energy Storage* **2020**, *27*, No. 101047.

(30) Carrillo, A. J.; González-Aguilar, J.; Romero, M.; Coronado, J. M. Solar Energy on Demand: A Review on High Temperature Thermochemical Heat Storage Systems and Materials. *Chem. Rev.* **2019**, *119*, 4777−4816.

(31) Chan, M. S. C.; Marek, E.; Scott, S. A.; Dennis, J. S. Chemical Looping Epoxidation. *J. Catal.* **2018**, *359*, 1−7.

(32) Zoller, S.; Koepf, E.; Nizamian, D.; Stephan, M.; Patané, A.; Haueter, P.; Romero, M.; González-Aguilar, J.; Lieftink, D.; de Wit, E.; Brendelberger, S.; Sizmann, A.; Steinfeld, A. A Solar Tower Fuel Plant for the Thermochemical Production of Kerosene from $H_2O$ and $CO_2$. *Joule* **2022**, *6*, 1606−1616.

(33) Yashima, M.; Morimoto, K.; Ishizawa, N.; Yoshimura, M. Diffusionless Tetragonal−Cubic Transformation Temperature in Zirconia−Ceria Solid Solutions. *J. Am. Ceram. Soc.* **1993**, *76*, 2865−2868.

(34) Sánchez Escribano, V.; López, E. F.; Panizza, M.; Resini, C.; Amores, J. M. G.; Busca, G. Characterization of Cubic Ceria−Zirconia Powders by X-ray Diffraction and Vibrational and Electronic Spectroscopy. *Solid State Sci.* **2003**, *5*, 1369−1376.

(35) Yashima, M.; Arashi, H.; Kakihana, M.; Yoshimura, M. Raman Scattering Study of Cubic−Tetragonal Phase Transition in $Zr_{1-x}Ce_xO_2$ Solid Solution. *J. Am. Ceram. Soc.* **1994**, *77*, 1067−1071.

(36) Zhang, F.; Chen, C.-H.; Hanson, J. C.; Robinson, R. D.; Herman, I. P.; Chan, S.-W. Phases in Ceria−Zirconia Binary Oxide $(1-x)CeO_2$−$xZrO_2$ Nanoparticles: The Effect of Particle Size. *J. Am. Ceram. Soc.* **2006**, *89*, 1028−1036.

(37) Yin, K.; Davis, R. J.; Mahamulkar, S.; Jones, C. W.; Agrawal, P.; Shibata, H.; Malek, A. Catalytic Oxidation of Solid Carbon and Carbon Monoxide over Cerium-Zirconium Mixed Oxides. *AIChE J.* **2017**, *63*, 725−738.

(38) Pechini, M. P. Method of Preparing Lead and Alkaline Earth Titanates and Niobates and Coating Method Using the Same to Form a Capacitor. U.S. Patent 3,330,697, 1967.

(39) Yashima, M.; Ohtake, K.; Kakihana, M.; Yoshimura, M. Synthesis of Metastable Tetragonal ($t'$) Zirconia−Ceria Solid Solutions by the Polymerized Complex Method. *J. Am. Ceram. Soc.* **1994**, *77*, 2773−2776.

(40) Petkovich, N. D.; Rudisill, S. G.; Venstrom, L. J.; Boman, D. B.; Davidson, J. H.; Stein, A. Control of Heterogeneity in Nanostructured $Ce_{1-x}Zr_xO_2$ Binary Oxides for Enhanced Thermal Stability and Water Splitting Activity. *J. Phys. Chem. C* **2011**, *115*, 21022−21033.

(41) Zhao, Z.; Uddi, M.; Tsvetkov, N.; Yildiz, B.; Ghoniem, A. F. Redox Kinetics and Nonstoichiometry of $Ce_{0.5}Zr_{0.5}O_{2-\delta}$ for Water Splitting and Hydrogen Production. *J. Phys. Chem. C* **2017**, *121*, 11055−11068.

(42) Zhao, Z.; Uddi, M.; Tsvetkov, N.; Yildiz, B.; Ghoniem, A. F. Enhanced Intermediate-Temperature $CO_2$ Splitting Using Non-stoichiometric Ceria and Ceria−Zirconia. *Phys. Chem. Chem. Phys.* **2017**, *19*, 25774−25785.

(43) Boudart, M. *Kinetics of Chemical Processes*; Prentice-Hall, 1968.

(44) Deen, W. M. *Analysis of Transport Phenomena*, 2nd ed.; Oxford University Press, 2012.




https://doi.org/10.1021/acs.jpcc.2c08117
J. Phys. Chem. C 2023, 127, 2936−2952

(45) Einstein, A. *Investigations on the Theory of the Brownian Movement*; Dover Publications, 1956.
(46) Crank, J. *The Mathematics of Diffusion*, 2nd ed.; Clarendon Press, 1975.
(47) Murch, G. E. The Exact Nernst-Einstein Equations and the Interpretation of Cross Phenomenological Coefficients in Unary, Binary, and Ambipolar Systems. *Radiat. Eff.* **1983**, *73*, 299−305.
(48) Aris, R. On Shape Factors for Irregular Particles—I: The Steady State Problem. Diffusion and Reaction. *Chem. Eng. Sci.* **1957**, *6*, 262−268.
(49) Chase, M. W., Jr. *NIST-JANAF Thermochemical Tables*, 4th Ed.; *J. Phys. Chem. Ref. Data* 1998, Monograph 9.
(50) Hori, C. E.; Brenner, A.; Simon Ng, K. Y.; Rahmoeller, K. M.; Belton, D. Studies of the Oxygen Release Reaction in the Platinum−Ceria−Zirconia System. *Catal. Today* **1999**, *50*, 299−308.
(51) Li, C.; Chen, Y.; Li, W.; Xin, Q. Spillover of Atomic Oxygen and Reverse Spillover of Dioxygen Species on Pt/$CeO_2$ Catalyst. In *Studies in Surface Science and Catalysis*; Inui, T.; Fujimoto, K.; Uchijima, T.; Masai, M., Eds.; Elsevier, 1993; Vol. *77*, pp 217−222.
(52) Tang, W.; Hu, Z.; Wang, M.; Stucky, G. D.; Metiu, H.; McFarland, E. W. Methane Complete and Partial Oxidation Catalyzed by Pt-Doped $CeO_2$. *J. Catal.* **2010**, *273*, 125−137.
(53) Zafiris, G. S.; Gorte, R. J. Evidence for Low-Temperature Oxygen Migration from Ceria to Rh. *J. Catal.* **1993**, *139*, 561−567.
(54) Brewer, L. Thermodynamic Properties of the Oxides and their Vaporization Processes. *Chem. Rev.* **1953**, *52*, 1−75.
(55) Li, C.; Domen, K.; Maruya, K.; Onishi, T. Dioxygen Adsorption on Well-Outgassed and Partially Reduced Cerium Oxide Studied by FT-IR. *J. Am. Chem. Soc.* **1989**, *111*, 7683−7687.
(56) Li, C.; Domen, K.; Maruya, K.; Onishi, T. Oxygen Exchange Reactions over Cerium-Oxide: An FT-IR Study. *J. Catal.* **1990**, *123*, 436−442.
(57) Soria, J.; Coronado, J. M.; Consea, J. C. Spectroscopic Study of Oxygen Adsorption on $CeO_2/\gamma$-$Al_2O_3$ Catalyst Supports. *J. Chem. Soc., Faraday Trans.* **1996**, *92*, 1619−1626.
(58) Descorme, C.; Madier, Y.; Duprez, D. Infrared Study of Oxygen Adsorption and Activation on Cerium−Zirconium Mixed Oxides. *J. Catal.* **2000**, *196*, 167−173.
(59) Martínez-Arias, A.; Fernández-García, M.; Belver, C.; Conesa, J. C.; Soria, J. EPR Study on Oxygen Handling Properties of Ceria, Zirconia, and Zr−Ce (1:1) Mixed Oxide Samples. *Catal. Lett.* **2000**, *65*, 197−204.
(60) Pushkarev, V. V.; Kovalchuk, V. I.; d'Itri, J. L. Probing Defect Sites on the $CeO_2$ Surface with Dioxygen. *J. Phys. Chem. B* **2004**, *108*, 5341−5348.
(61) Wu, Z.; Li, M.; Howe, J.; Meyer, H. M.; Overbury, S. H. Probing Defect Sites on $CeO_2$ Nanocrystals with Well-Defined Surface Planes by Raman Spectroscopy and $O_2$ Adsorption. *Langmuir* **2010**, *26*, 16595−16606.





https://doi.org/10.1021/acs.jpcc.2c08117
*J. Phys. Chem. C* 2023, 127, 2936−2952